Estuarine, Coastal and Shelf Science 117 (2013) 107–124

Contents lists available at SciVerse ScienceDirect

Estuarine, Coastal and Shelf Science

journal homepage: www.elsevier.com/locate/ecss

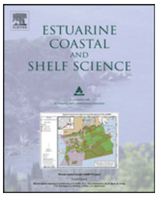

Sediment flux modeling: Calibration and application for coastal systems

Damian C. Brady[a,*], Jeremy M. Testa[b], Dominic M. Di Toro[c], Walter R. Boynton[d], W. Michael Kemp[b]

[a] School of Marine Sciences, University of Maine, 193 Clark Cove Road, Walpole, ME 04573, USA
[b] Horn Point Laboratory, University of Maryland Center for Environmental Science, 2020 Horns Point Rd., Cambridge, MD 21613, USA
[c] Department of Civil and Environmental Engineering, University of Delaware, 356 DuPont Hall, Newark, DE 19716, USA
[d] Chesapeake Biological Laboratory, University of Maryland Center for Environmental Science, P.O. Box 38, Solomons, MD 20688, USA

ARTICLE INFO

Article history:
Received 19 June 2012
Accepted 7 November 2012
Available online 21 November 2012

Keywords:
sediments
modeling
Chesapeake Bay
ammonium
sediment oxygen demand
diagenesis

ABSTRACT

Benthic–pelagic coupling in shallow estuarine and coastal environments is an important mode of particle and solute exchange and can influence lag times in the recovery of eutrophic ecosystems. Links between the water column and sediments are mediated by particulate organic matter (POM) deposition to the sediment and its subsequent decomposition. Some fraction of the regenerated nutrients are returned to the water column. A critical component in modeling sediment fluxes is the organic matter flux to the sediment. A method is presented for estimating POM deposition, which is especially difficult to measure, by using a combination of long term time series of measured inorganic nutrient fluxes and a mechanistic sediment flux model (SFM). A Hooke–Jeeves pattern search algorithm is used to adjust organic matter deposition to fit ammonium (NH_4^+) flux at 12 stations in Chesapeake Bay for up to 17 years.

POM deposition estimates matched reasonably well with sediment trap estimates on average (within 10%) and were strongly correlated with previously published estimates based upon sediment chlorophyll-*a* (chl-*a*) distribution and degradation. Model versus field data comparisons of NH_4^+ flux, sediment oxygen demand (SOD), sulfate (SO_4^{2-}) reduction rate, porewater NH_4^+, and sedimentary labile carbon concentrations further validated model results and demonstrated that SFM is a powerful tool to analyze solute fluxes. Monthly model-field data comparisons clearly revealed that POM decomposition in the original SFM calibration was too rapid, which has implications for lagged ecosystem responses to nutrient management efforts. Finally, parameter adjustments have been made that significantly improve model-field data comparisons and underscore the importance of revisiting and recalibrating models as long time series (>5 years) become available.

1. Introduction

Strong coupling between pelagic and benthic habitats is a fundamental feature of most shallow coastal aquatic ecosystems (Nixon, 1981; Kamp-Nielsen, 1992; Kemp and Boynton, 1992; Soetaert and Middelburg, 2009). A primary mechanism that connects benthic and pelagic habitats is the downward transport of organic material, which may be composed of senescent algal cells, zooplankton fecal pellets, and relatively refractory organic compounds imported from marshes or rivers. Organic matter that reaches the sediment drives sediment biogeochemical processes and resultant nutrient fluxes (Jensen et al., 1990), feeds benthic organisms (Heip et al., 1995), and can control sediment oxygen demand (Kemp and Boynton, 1992). Despite the importance of particulate organic matter (POM) deposition to coastal sediment processes, few direct measurements have been made because of the inherent difficulty in deriving depositional rates from sediment traps (e.g., Buesseler et al., 2007), especially in shallow coastal waters where resuspended sediment material can accumulate in traps (Kemp and Boynton, 1984; Hakanson et al., 1989; Kozerski, 1994; Gust and Kozerski, 2000).

Eutrophication is a common phenomenon in coastal aquatic ecosystems where increased nutrient loading from the adjacent watershed promotes increased phytoplankton growth that degrades water quality (e.g. hypoxia and harmful algal blooms, Cloern, 2001; Diaz and Rosenberg, 2008; Nixon, 1995). Typically, nutrient stimulated phytoplankton growth leads to higher rates of POM deposition, and thus higher rates of sediment oxygen demand (SOD) and sediment–water nutrient fluxes (e.g., Kelly and Nixon, 1984; Kelly et al., 1985). Eutrophication mitigation via reductions

---

* Corresponding author.
E-mail address: damian.brady@maine.edu (D.C. Brady).

0272-7714/$ – see front matter © 2012 Elsevier Ltd. All rights reserved.
http://dx.doi.org/10.1016/j.ecss.2012.11.003

in nutrient and organic carbon loads to estuaries has become a goal of most water management agencies (Boesch et al., 2001; Conley et al., 2002). To evaluate and predict the consequences of such eutrophication mitigation strategies, observational data are linked to models of varying complexity that include linked hydrodynamic and biogeochemical processes, including sediment process models (Cerco and Cole, 1993; Lin et al., 2007).

In shallow coastal ecosystems, the need for sediment process models is especially important. In very shallow ecosystems (<5 m), sediments may be populated by submerged vascular plants and/or benthic algal communities, both of which modify sediment biogeochemical reactions via nutrient uptake and sediment oxygenation (Miller et al., 1996; McGlathery et al., 2007). In moderately shallow systems (5–50 m), pelagic–benthic coupling involves sediments as sites for high rates of nutrient recycling (Cowan et al., 1996) and oxygen consumption (Kemp et al., 1992). Depleted bottom-water O_2, a common feature of eutrophication, complicates predictions of sediment nutrient exchange because low O_2 concentrations exert control over sediment biogeochemical reactions (Middelburg and Levin, 2009; Testa and Kemp, 2012). Models of sediment diagenetic processes can be used to simulate exchanges of particulate and dissolved substances between the water column and sediments. Such models are particularly useful to simulate nutrient storage in sediments and resulting delays in ecosystem recovery following eutrophication abatement (Conley et al., 2009; Soetaert and Middelburg, 2009).

In general, sediment process model structures range from relatively simple empirical relationships to more complex process simulations that include time-varying state variables (Boudreau, 1991b; Cerco and Noel, 2005). Simple model representations include assigning a constant O_2 or nutrient sediment–water flux (e.g., Scully, 2010) or using basic parameterizations of sediment–water flux as a function of overlying water conditions (Fennel et al., 2006; Hetland and DiMarco, 2008). More complex process models may simulate one or two layers, each of which represent a particular chemical environment, and such models tend to demand limited computational effort (Emerson et al., 1984; Di Toro, 2001). Process models may also resolve depth into several layers, allowing for simulations of pore-water constituent vertical profiles (Boudreau, 1991a; Dhakar and Burdige, 1996; Soetaert et al., 1996; Cai et al., 2010). Depth resolution in such complex models is usually associated with high computational demand, therefore less vertically-resolved models are commonly used when sediment biogeochemical models are coupled to water column models (Cerco and Noel, 2005; Sohma et al., 2008).

A sediment biogeochemical model was developed to link to spatially articulated water column models describing biogeochemical processes at a limited computational cost (Di Toro, 2001). This sediment flux model (SFM) separates sediment reactions into two layers and generates fluxes of key solutes (e.g., nitrogen, phosphorus, silica, dissolved oxygen (O_2), sulfide, and methane). SFM has been successfully integrated into water quality models in many coastal systems, including Massachusetts Bay (Jiang and Zhou, 2008), Chesapeake Bay (Cerco and Cole, 1993; Cerco, 1995; Cerco and Noel, 2005), Delaware's Inland Bays (Cerco and Seitzinger, 1997), and Long Island Sound (Di Toro, 2001). SFM can also be used as a stand-alone diagnostic tool in sediment process studies, especially over seasonal to decadal time scales. For example, it has been used to simulate sediment dynamics in the Rhode Island Marine Ecosystem Research Laboratory (MERL) mesocosms (Di Toro and Fitzpatrick, 1993; Di Toro, 2001). Such a stand-alone sediment modeling tool, when combined with high-quality time series observations, can be used for parameter optimization, scenario analysis, and process investigations. We direct the reader to Di Toro (2001) for a comprehensive description of the development, calibration, theory, and application of SFM.

The purpose of this study is to: (1) utilize a stand-alone version of SFM to support and analyze sediment process observations at a variety of Chesapeake Bay stations; (2) use SFM to estimate organic matter deposition to sediments in Chesapeake Bay; and (3) calibrate and validate SFM predictions with a multi-decadal time-series of water column concentrations and sediment–water exchanges of nutrients and O_2 at 12 stations in Chesapeake Bay. We focus our process studies on NH_4^+, NO_3^- and O_2 fluxes. SFM also computes phosphorus and silica fluxes and the calibration and validation of these fluxes will be the focus of a companion paper (Testa et al., in press). It is suggested that SFM can serve as a widely applicable tool for a variety of coastal ecosystems to aid in sediment processes and water quality investigations.

2. Methods

SFM was previously calibrated and validated in Chesapeake Bay for the years 1985–1988, using sediment–water flux and overlying-water nutrient and O_2 data that were available at that time for 8 sites (Chapter 14 in Di Toro, 2001). More than two decades later, data availability has expanded. New calibration and validation can improve SFM simulation skill for Chesapeake Bay and can demonstrate its utility as a stand-alone tool available for use in other systems. In this paper we describe and analyze SFM performance in the upper portion of Chesapeake Bay using field data from 12 stations (Fig. 1) over 4–17 year time series. SFM can be run on a personal computer, executing a 25-year run on the time-

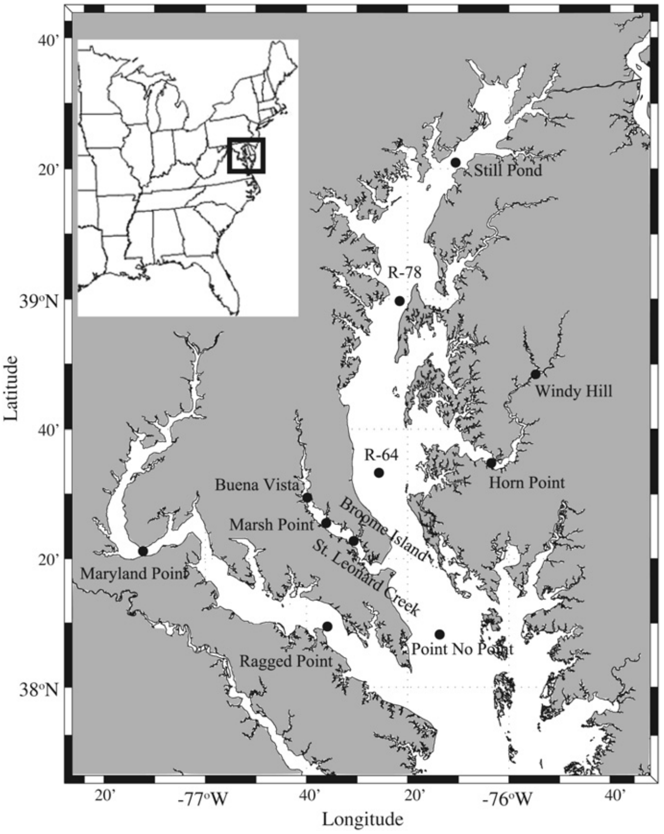

Fig. 1. Map of northern Chesapeake Bay, on the east coast of the United States (inset), showing the locations where sediment flux model (SFM) simulations were compared to Sediment Oxygen and Nutrient Exchange (SONE) observations.

scale of seconds, and a MATLAB interface is available for input generation, model execution, post-processing, and plotting.

2.1. General model description

What follows is a brief summary of the structure and initial calibration of SFM (Di Toro and Fitzpatrick, 1993; Di Toro, 2001). The modeling framework encompasses three processes: (1) the sediment receives depositional fluxes of particulate organic carbon and nitrogen from the overlying water; (2) the mineralization of particulate organic matter produces soluble intermediates that are quantified as diagenesis fluxes; and (3) solutes react in the aerobic and anaerobic layers of the sediment and portions are returned to the overlying water (Fig. 2). The model assumes that organic matter mineralization is achieved by denitrification, sulfate reduction, and methanogenesis. Carbon is first utilized by denitrification (which is calculated independently) and any remaining carbon is processed by sulfate reduction until SO_4^{2-} becomes limiting, after which methanogenesis occurs. To model these processes, SFM numerically integrates mass-balance equations for chemical constituents in two functional layers: an aerobic layer near the sediment water interface of variable depth (H_1) and an anaerobic layer below that is equal to the total sediment depth (10 cm) minus the depth of H_1 (Figs. 2–4). The SFM convention is to use “0” when referring to the overlying water, “1” when referring to the aerobic layer, and “2” when referring to the anaerobic layer. A strict mass-balance approach is used to compute temporal changes in concentrations of particulate and dissolved constituents, which in turn produce fluxes across the volume boundaries.

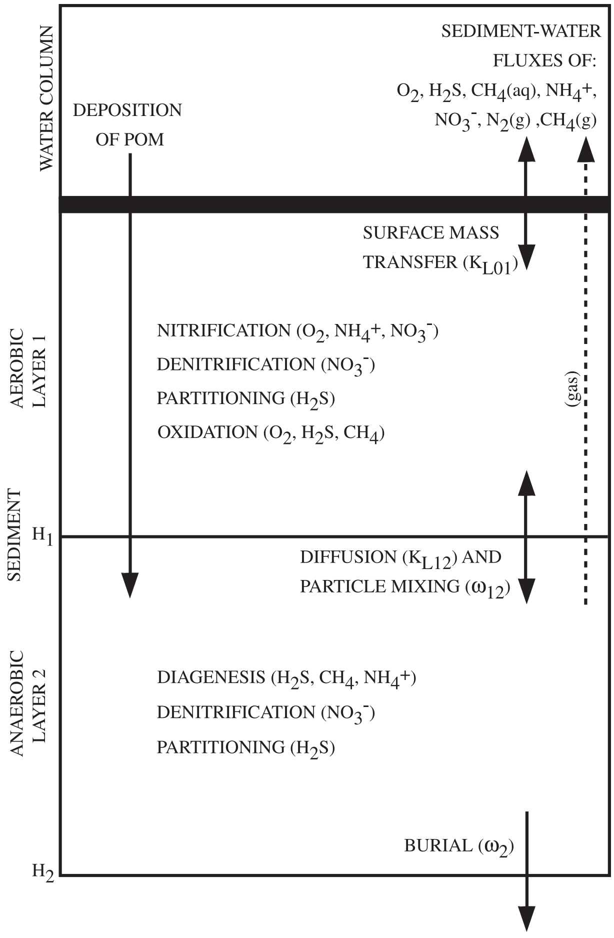

Fig. 2. Generic schematic diagram of the sediment flux model (SFM), including state variables, transport and biogeochemical processes, and boundary conditions. Note that the depths of the aerobic (H_1) and anaerobic (H_2) layers vary over time.

The general forms of the equations are presented in Table 1 (Eqs. (1) and (2)). For example, one can replace C_{T1} with $NH_{4,1}$ to compute the change in NH_4^+ concentration in the aerobic layer (Eq. (1) in Table 1). The governing equations are mass balance equations that include biogeochemical reactions $((\kappa_1^2/K_{L01})C_{T1})$ and dissolved and particulate mixing (i.e., burial; $\omega_2 C_{T1}$, diffusion of dissolved material from the overlying water column; $K_{L01}(f_{d0}C_{T0} - f_{d1}C_{T1})$ and between layers; $K_{L12}(f_{d2}C_{T2} - f_{d1}C_{T1})$, and mixing of particulate material between layers;$\omega_{12}(f_{p2}C_{T2} - f_{p1}C_{T1})$: see Eqs. (1) and (2) in Table 1).

Dissolved O_2 concentrations are not modeled as a state variable in SFM, but concentrations in each layer are determined as follows. In layer 2, the anaerobic layer, $O_2(2)$ is assumed to be zero. Because $O_2(0)$, the overlying water concentration, is a boundary condition, a linear decline is assumed from $O_2(0)$ to zero ($O_2(2)$) in the aerobic layer, thus $O_2(1) = (O_2(0) + O_2(2))/2 = O_2(0)/2$.

A key to this model is an algorithm that continually updates the thickness of the aerobic layer, H_1, by computing the product of the diffusion coefficient (D_{O_2}) and the ratio of overlying-water O_2 concentration ($[O_2(0)]$) to sediment oxygen demand (SOD).

$$H_1 = D_{O_2}\frac{[O_2(0)]}{\mathrm{SOD}} \tag{1}$$

This relationship was perhaps first suggested by Grote (1934) – quoted by Hutchinson (1957) – and verified by measurements (Jorgensen and Revsbech, 1985; Cai and Sayles, 1996). The inverse of the second term on the right hand side of Equation (1) is the surface mass transfer coefficient ($K_{L01} = (\mathrm{SOD}/[O_2(0)]) = (D_{O_2}/H_1)$; Eq. (5) in Table 1). The surface mass transfer coefficient controls solute exchange between the aerobic layer and the overlying water column. The model uses the same mass transfer coefficient for all solutes since differences in the diffusion coefficients between solutes are subsumed in the kinetic parameters that are fit to data (Chapter 3 in Di Toro, 2001; Fennel et al., 2009). The SOD in Equation (1), which is computed as described below, also depends on the thickness of the aerobic layer. Therefore, the equation for SOD is nonlinear. It is solved numerically at each time step of the simulation.

Dissolved and particle mixing between layers 1 and 2 (K_{L12} and ω_{12}, Eqs. (6) and (7) in Table 1) are modeled as a function of passive transport and proxies for the activities of benthic organisms. K_{L12} enhancement due to benthic activity is parameterized directly, that is, the dissolved mixing coefficient (D_d) was increased such that K_{L12} is 2–3 times molecular diffusion (Matisoff and Wang, 1998). The rate of mixing of sediment particles (ω_{12}; Eq. (7) in Table 1) by macrobenthos is quantified by estimating the apparent particle diffusion coefficient (D_p; Chapter 13 in Di Toro, 2001). In the model, particle mixing is controlled by temperature (1st term in Eq. (7) in Table 1; Balzer, 1996), carbon input (2nd term in Eq. (7) in Table 1; Robbins et al., 1989), and oxygen (3rd term in Eq. (7) in Table 1; Diaz and Rosenberg, 1995). In order to make the model self-consistent, that is to use only internally-computed variables in the parameterizations, the model assumes that benthic biomass and therefore, particle mixing is correlated with the amount of labile carbon (e.g., POC_1) present in the sediment. However, if excess carbon loading creates unfavorable oxygen conditions, the model accumulates this as benthic stress (S in Eq. (7) in Table 1). As O_2 decreases, $1 - k_S S$ approaches zero. After the stress has passed, the minimum is carried forward for the rest of the year in order to simulate the observation that benthic communities do not recover until the following year (Diaz and Rosenberg, 1995).

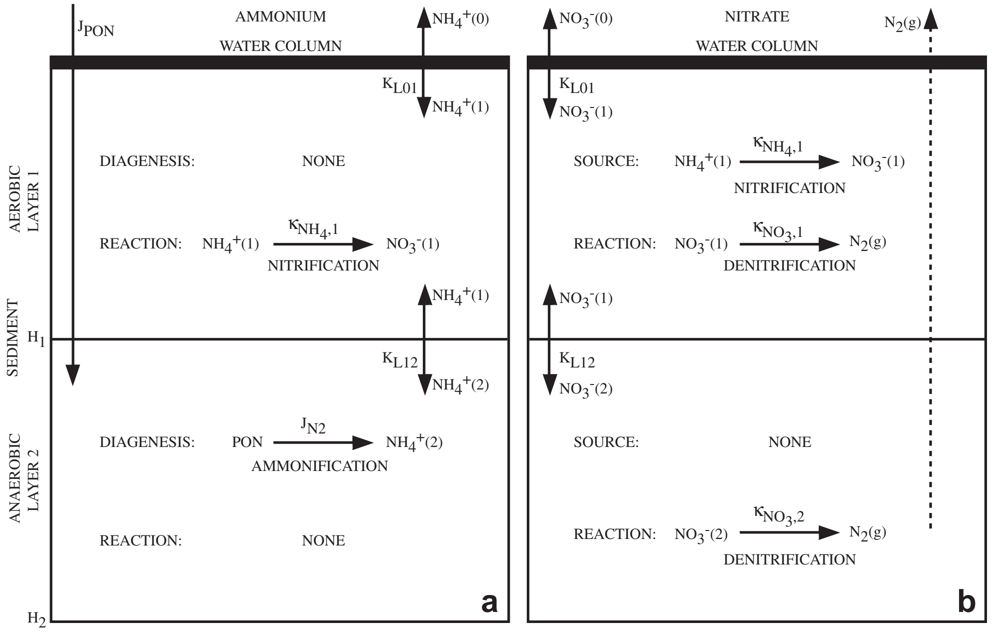

Fig. 3. Schematic representation of nitrogen transport and kinetics in the sediment flux model (SFM). Panels a & b represent the dynamics of the NH_4^+ and NO_3^- models, respectively. Note: (1) there is no diagenesis (ammonification) in layer 1 (panel a). (2) there is no source of nitrate in the anaerobic layer, as no O_2 is present (Panel b).

2.2. Ammonium flux

NH_4^+ concentrations are computed for both aerobic and anaerobic layers via mass balances of biogeochemical and physical processes. Fig. 3a shows the sources and sinks of NH_4^+ in the model. NH_4^+ is produced by organic matter diagenesis (J_{N2} in Fig. 3a, J_{T2} in Eq. (10) in Table 1) in the anaerobic layer, while in the aerobic layer, NH_4^+ is converted to nitrate (NO_3^-) via nitrification via a first order reaction rate ($k_{NH_4^+,1}$) (Fig. 3a) with Monod kinetics (Eq. (8) in Table 1). Mass-transfer coefficients are employed to model diffusion of NH_4^+ between the anaerobic and aerobic layers (K_{L12}) and between the aerobic layer and the overlying water (K_{L01}).

Calculation of nitrification (i.e., the oxidation of NH_4^+ to NO_3^-) is a good example of a process that depends on the depth of H_1. The nitrification rate expression in the mass balance equations for NH_4^+ is a product of the aerobic layer nitrification rate ($k_{NH_4^+,1}$) and the depth of the aerobic layer (Fig. 3a):

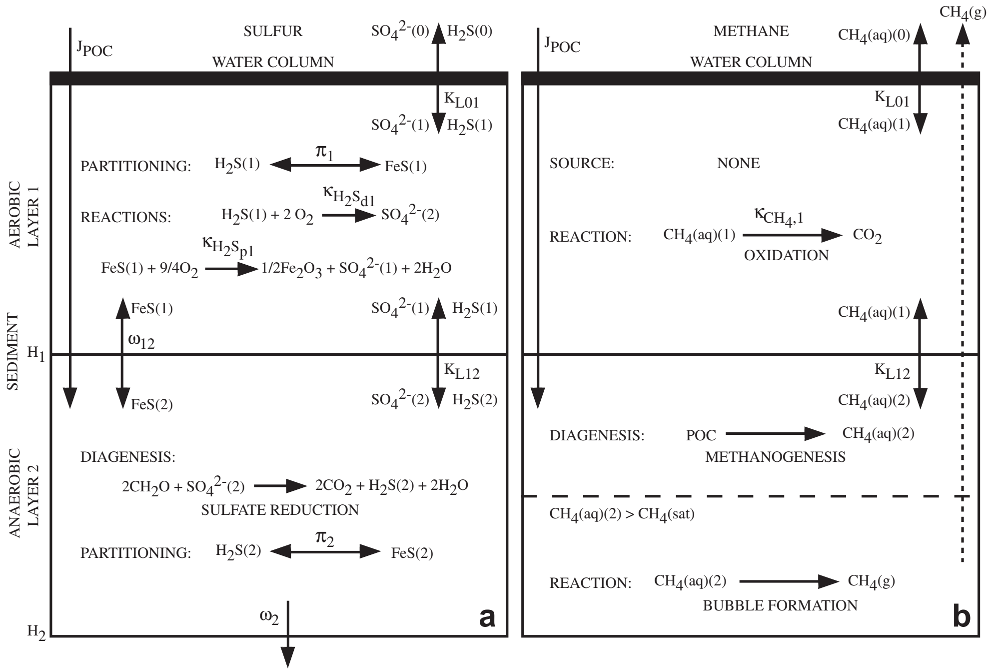

Fig. 4. Schematic representation of the sulfide model, with both solid and particulate phases and associated transport (Panel a), as well as the methane model which includes oxidation, diffusion, and bubble formation (Panel b). The oxygen uptake associated with these two models is added to nitrification-associated oxygen uptake to calculate sediment oxygen demand.

$$k_{\mathrm{NH}_4^+,1} H_1 = \frac{D_{\mathrm{NH}_4^+} k_{\mathrm{NH}_4^+,1}}{K_{L01}} \tag{2}$$

The product $D_{\mathrm{NH}_4^+} k_{\mathrm{NH}_4^+,1}$ is made up of two coefficients, neither of which is readily measured. The diffusion coefficient in a millimeter thick layer of sediment at the sediment water interface may be larger than the diffusion coefficient in the bulk of the sediment due to the effects of overlying water shear. It is therefore convenient to subsume two relatively unknown parameters into one parameter that is calibrated to data called $\kappa_{\mathrm{NH}_4^+,1}$ (Fig. 3a):

$$\kappa_{\mathrm{NH}_4,1} = \sqrt{D_{\mathrm{NH}_4^+} k_{\mathrm{NH}_4^+,1}} \tag{3}$$

which is termed the reaction velocity for NH_4 oxidation, since its dimensions are length per unit time. Nitrification is then computed as a function of $\kappa_{\mathrm{NH}_4,1}$, temperature, and NH_4^+ and O_2 limitation (Eq. (8) in Table 1).

The mass balance NH_4^+ equations for each layer are:

$$\begin{aligned}\frac{\mathrm{d}\left\{H_1\left[\mathrm{NH}_4^+(1)\right]\right\}}{\mathrm{d}t} = & -\frac{\kappa_{\mathrm{NH}_4,1}^2}{K_{L01}}\left[\mathrm{NH}_4^+(1)\right] - K_{L01}\left(\left[\mathrm{NH}_4^+(1)\right.\right. \\ & \left.\left. - \mathrm{NH}_4^+(0)\right]\right) + K_{L12}\left(\left[\mathrm{NH}_4^+(2) - \mathrm{NH}_4^+(1)\right]\right)\end{aligned} \tag{4}$$

$$\frac{\mathrm{d}\left\{H_2\left[\mathrm{NH}_4^+(2)\right]\right\}}{\mathrm{d}t} = -K_{L12}\left(\left[\mathrm{NH}_4^+(2) - \mathrm{NH}_4^+(1)\right]\right) + J_{N2} \tag{5}$$

where $\mathrm{NH}_4^+(0)$, $\mathrm{NH}_4^+(1)$, and $\mathrm{NH}_4^+(2)$ are the NH_4^+ concentrations in the overlying water, layer 1 and layer 2, respectively. Note that for NH_4^+, $\kappa_2 = 0$ and $J_{N1} = 0$. It should be noted that in the time varying solution, H_1 and H_2 are within the derivative since the depth of the layers are variable and can entrain and lose mass when they are changing (see Chapter 13 in Di Toro, 2001 for the method to account for these mass transfers). The depth of the anaerobic layer (H_2) is then calculated as the difference between the total sediment depth (10 cm) and H_1. Finally, the sediment–water NH_4^+ flux (denoted as $J[\mathrm{NH}_4^+]$) is equal to $K_{L01}([\mathrm{NH}_4^+(1) - \mathrm{NH}_4^+(0)])$. One important consequence of this equation is that the gradient in solute concentration between the sediment and the overlying water-column is not the sole control on solute flux during certain times of the year, as fluxes are primarily controlled by mixing via K_{L01}. Mixing is primarily controlled by temperature, overlying-water dissolved $[\mathrm{O}_2(0)]$, and the reactions that control the depth of the aerobic layer.

2.3. *Nitrate flux*

There are two sources of NO_3^- in SFM: (1) NO_3^- enters from the overlying water column as controlled by surface mass transfer and concentration gradient and (2) NH_4^+ is oxidized in the aerobic layer (i.e., nitrification) (Eq. (13) in Table 1, Fig. 3b; see Chapter 4 of Di Toro, 2001). In turn, NO_3^- can be returned to the overlying water column as NO_3^- flux ($J[\mathrm{NO}_3]$) or converted to nitrogen gas (i.e., denitrification, Eqs. (11) and (12) in Table 1). There is no biogeochemical nitrate source in the anaerobic layer (Fig. 3). Although unconventional (see Gypens et al., 2008 for a discussion of models of denitrification confined to the anaerobic layer), denitrification occurs in both the aerobic and anaerobic layers (Fig. 3b). The close coupling between nitrification and denitrification has been suggested by Blackburn et al. (1994) and there is considerable evidence for denitrification in the oxic layer, for example, within anoxic microsites (Jenkins and Kemp, 1984; Berg et al., 1998). The remainder of the formulation parallels the NH_4^+ flux model discussed in Section 3.2 and is diagrammed in Fig. 3b.

2.4. *Sulfate*

Sulfate reduction is an important diagenetic process in coastal marine sediments and is the source of sulfide, the oxidation of which is a large portion of SOD (Fig. 4a; Howarth and Jorgensen, 1984). Thus, SO_4^{2-} is explicitly modeled in SFM (Fig. 4a). SO_4^{2-} in the overlying water-column is calculated via a linear regression with overlying-water salinity. SO_4^{2-} is produced in the aerobic layer as a result of particulate and dissolved sulfide oxidation and removed in the anaerobic layer via sulfate reduction (Fig. 4a, Eq. (16) in Table 1). Because anaerobic layer SO_4^{2-} may become limiting to sulfate reduction in low-salinity sediments, the model computes a depth of SO_4^{2-} penetration (H_{SO_4}, Eq. (17) in Table 1). Since $\mathrm{SO}_4^{2-}(2) = 0$ at H_{SO_4} one can solve for H_{SO_4} using a one dimensional SO_4^{2-} mass balance equation in the anaerobic layer (Eq. (17) in Table 1; Chapter 11 in Di Toro (2001)). Because SO_4^{2-} is often less than the total sediment depth, K_{L12} is scaled to SO_4^{2-} to yield a SO_4^{2-} specific mass-transfer coefficient, $K_{L12,S}$ (Eq. (17) in Table 1).

2.5. *Sulfide*

The product of sulfate reduction in the anaerobic layer is dissolved sulfide ($\mathrm{H}_2\mathrm{S}$). Note that the carbon available for sulfate reduction is computed as the depositional flux of carbon minus the organic carbon utilized during denitrification (Eq. (16) in Table 1). SO_4^{2-} limitation on sulfide production (via sulfate reduction) is modeled via a Michaelis–Menten dependency on $\mathrm{SO}_4^{2-}(2)$ (Eq. (20) in Table 1). A portion of sulfide reacts with oxidized iron in the sediment to form particulate iron sulfide (FeS in Fig. 4a; Morse et al., 1987). SFM distinguishes between the solid and dissolved phases of sulfide via a layer-specific partition coefficient (Eqs. (3) and (4) in Table 1, Table 2). The oxidation of both particulate and dissolved sulfide is the product of a first-order kinetic constant ($\kappa_{\mathrm{H}_2\mathrm{S},d,p,1}^2$) and a linear dissolved O_2 dependency (Eq. (18) in Table 1) consistent with experimental data (Di Toro, 2001; Chapter 9).

2.6. *Methane*

Methanogenesis is computed as a fraction of total diagenesis, which is controlled by anaerobic-layer SO_4^{2-} (Eqs. (20) and (23) in Table 1). For example, methanogenesis is equal to total diagenesis when $\mathrm{SO}_4^{2-}(2)$ is extremely low relative to the constant K_{M,SO_4} (Eq. (23) in Table 1). The dissolved methane ($[\mathrm{CH}_4]$ (aq)) produced by carbon diagenesis can either be oxidized in the aerobic layer via the product of a first-order reaction constant and Michaelis–Menten O_2 dependency (Fig. 4b, Eq. (21) in Table 1), released as a flux to the overlying water column, or becomes gaseous ($J[\mathrm{CH}_4]$ (g)) when its concentration exceeds saturation ($[\mathrm{CH}_4]$(sat); Fig. 4b and Eq. (24) in Table 1). $J[\mathrm{CH}_4]$(g) is computed via a mass-balance of CH_4(aq) sources and sinks when $\mathrm{CH}_4(\mathrm{aq}) \geq \mathrm{CH}_4(\mathrm{sat})$ (Eq. (24) in Table 1).

2.7. *Sediment oxygen demand*

Sediment oxygen demand (SOD) is computed by summing all model processes that consume molecular O_2, including the oxidation of NH_4^+ (nitrogenous SOD = NSOD; Eqs. (28) and (29) in Table 1) and the oxidation of dissolved sulfide + particulate sulfide ($\mathrm{SOD}_{\mathrm{H}_2\mathrm{S}}$) and dissolved methane ($\mathrm{SOD}_{\mathrm{CH}_4}$). Carbonaceous SOD (CSOD) is equivalent to $\mathrm{SOD}_{\mathrm{H}_2\mathrm{S}} + \mathrm{SOD}_{\mathrm{CH}_4}$ (Eqs. (25)–(27) in Table 1). In the case of the sulfur and methane models, all solutes are modeled in units of stoichiometric O_2 equivalents (O_2^*, Tables 1 and 2). This model formulation allows the model to track reduced end-products (e.g., sulfide) in the summer for re-oxidization during the winter, a potentially important process when determining the lag between loading and sediment recovery.

Table 1
The model equations are listed below. The solutions are found by numerically integrating the equations (Di Toro, 2001). Parameter definitions are located at the bottom of this table.[a]

	Mass balance equations (these are the general equations for C_{T1} and C_{T2}):
1	$\frac{d\{H_1 C_{T1}\}}{dt} = -\frac{\kappa_1^2}{K_{L01}} C_{T1} + K_{L01}(f_{d0} C_{T0} - f_{d1} C_{T1}) + \omega_{12}(f_{p2} C_{T2} - f_{p1} C_{T1}) + K_{L12}(f_{d2} C_{T2} - f_{d1} C_{T1}) - \omega_2 C_{T1} + J_{T1}$
2	$\frac{d\{H_2 C_{T2}\}}{dt} = -\kappa_2 C_{T2} - \omega_{12}(f_{p2} C_{T2} - f_{p1} C_{T1}) - K_{L12}(f_{d2} C_{T2} - f_{d1} C_{T1}) + \omega_2 (C_{T1} - C_{T2}) + J_{T2}$
3	where: $f_{di} = \frac{1}{1 + m_i \pi_i} \quad i = 1, 2$
4	$f_{pi} = 1 - f_{di}$
5	$K_{L01} = \frac{D_{O_2}}{H_1} = \frac{\mathrm{SOD}}{[O_2(0)]}$
6	$K_{L12} = \frac{D_d \theta_{D_d}^{(T-20)}}{(H_1 + H_2)/2}$
7	$\omega_{12} = \frac{D_p \theta_{D_p}^{(T-20)}}{H_1 + H_2} \frac{\mathrm{POC}_1}{\mathrm{POC}_R} (1 - k_s S) \min_{(\text{each year})}$ where $\frac{dS}{dt} = -k_s S + \frac{K_{M,D_p}}{K_{M,D_p} + [O_2(0)]/2}$
	The kinetic and source terms for the ammonium, nitrate, sulfide, methane, and oxygen systems are listed next.
	Ammonium (NH_4^+)
8	$\kappa_1^2 = \kappa_{NH_4,1}^2 \theta_{NH_4}^{(T-20)} \left(\frac{K_{M,NH_4} \theta_{K_{M,NH_4}}^{(T-20)}}{K_{M,NH_4} \theta_{K_{M,NH_4}}^{(T-20)} + [NH_4(1)]} \right) \left(\frac{[O_2(0)]/2}{K_{M,NH_4,O_2} + [O_2(0)]/2} \right)$
9	$\kappa_2 = 0$
10	$J_{T1} = 0$ $J_c = \sum_{i=1}^{2} -k_{POC,i} \theta_{POC,i}^{(T-20)} \mathrm{POC}_i H_2$ $J_{T2} = a_{N,C} J_c$
	Nitrate (NO_3^-)
11	$\kappa_1^2 = \kappa_{NO_3,1}^2 \theta_{NO_3}^{(T-20)}$
12	$\kappa_2 = \kappa_{NO_3,2} \theta_{NO_3}^{(T-20)}$
13	$J_{T1} = \kappa_{NH_4,1}^2 \theta_{NH_4}^{(T-20)} \frac{[NH_4(1)]}{K_{L01}} \left(\frac{K_{M,NH_4} \theta_{K_{M,NH_4}}^{(T-20)}}{K_{M,NH_4} \theta_{K_{M,NH_4}}^{(T-20)} + [NH_4(1)]} \right) \left(\frac{[O_2(0)]/2}{K_{M,NH_4,O_2} [O_2(0)]/2} \right)$ $J_{T2} = 0$
	Sulfate (SO_4^{2-})
14	$\kappa_1^2 = 0$
15	$\kappa_2 = 0$
16	$J_{T1} = (\kappa_{H_2S,d1}^2 f_{d1} + \kappa_{H_2S,p1}^2 f_{p1}) \ \theta_{H_2S}^{(T-20)} \frac{[\sum H_2S(1)]}{K_{L01}} \frac{[O_2(0)]/2}{K_{M,H_2S,O_2}}$ $J_S = a_{O_2,C} J_C - a_{O_2,NO_3} \left(\frac{\kappa_{NO_3,1}^2 \theta_{NO_3}^{(T-20)}}{K_{L01}} [NO_3(1)] + \kappa_{NO_3,2} \theta_{NO_3}^{(T-20)} [NO_3(2)] \right)$ $J_{T2} = -J_S \frac{[SO_4(2)]}{[SO_4(2)] + K_{M,SO_4}}$
17	$H_{SO_4} = \sqrt{\frac{2 D_{SO_4} \theta_{D_p}^{(T-20)} [SO_4(0)] (H_1 + H_2)}{J_S}}$ If $H_{SO_4} < (H_1 + H_2)$: $K_{L12,S} = K_{L12} \frac{H_2}{H_{SO_4}}$
	Sulfide ($\sum H_s S$)
18	$\kappa_1^2 = (\kappa_{H_2S,d1}^2 f_{d1} + \kappa_{H_2S,p1}^2 f_{p1}) \ \theta_{H_2S}^{(T-20)} \frac{[O_2(0)]/2}{K_{M,H_2S,O_2}}$
19	$\kappa_2 = 0$
20	$J_{T1} = 0$ $J_{T2} = J_S \left(1 - \frac{K_{M,SO_4}}{([SO_4(2)] + K_{M,SO_4})} \right)$
	Methane (CH_4)
21	$\kappa_1^2 = \kappa_{CH_4,1}^2 \theta_{CH_4}^{(T-20)} \frac{[O_2(0)]/2}{K_{M,CH_4 O_2} + [O_2(0)]/2}$
22	$\kappa_2 = 0$

Table 1 (*continued*)

	Mass balance equations (these are the general equations for C_{T1} and C_{T2}):
23	$J_{T1} = 0$ $J_{T2} = J_S \dfrac{K_{M,SO_4}}{([SO_4(2)] + K_{M,SO_4})}$
24	If $CH_4(2)(aq) > CH_4(sat)$[a]: $J[CH_4(g)] = J_{T2} - K_{L01}([CH_4(1)(aq)] - [CH_4(0)(aq)]) - \dfrac{\kappa_1^2}{K_{L01}}[CH_4(1)(aq)]$
	Oxygen
25	$CSOD_{H_2S} = \dfrac{(\kappa_{H_2S,d1}^2 f_{d1} + \kappa_{H_2S,p1}^2 f_{p1})\theta_{H_2S}^{(T-20)}}{K_{L01}} \dfrac{[O_2(0)]/2}{K_{M,H_2S,O_2}}[\sum H_2S(1)]$
26	$CSOD_{CH_4} = \dfrac{\kappa_{CH_4}^2 \theta_{CH_{4,1}}^{(T-20)}}{K_{L01}} \dfrac{[O_2(0)]/2}{K_{M,CH_4O_2} + [O_2(0)]/2}[CH_4(1)(aq)]$
27	$CSOD = CSOD_{H_2S} + CSOD_{CH_4}$
28	$NSOD = a_{O_2,NH_4}\kappa_{NH_4,1}^2 \theta_{NH_4}^{(T-20)} \dfrac{[NH_4(1)]}{K_{L01}} \left(\dfrac{K_{M,NH_4}\theta_{K_{M,NH_4}}^{(T-20)}}{K_{M,NH_4}\theta_{K_{M,NH_4}}^{(T-20)} + [NH_4(1)]}\right)\left(\dfrac{[O_2(0)]/2}{K_{M,NH_4O_2} + [O_2(0)]/2}\right)$
29	$SOD = NSOD + CSOD$

[a] H_1, H_2 = depth of layer 1 and 2 (cm, see Chapter 13 in Di Toro (2001) for discussion of entrainment flux due to time-varying-sediment depth); C_{T0}, C_{T1}, C_{T2} = total (dissolved + particulate) concentration in layers (mmol m^{-3}); POC_1 = Layer 1 particulate organic carbon concentration (mmol m^{-3}), POC_R = reference particulate organic carbon concentration (0.1 mg C g solids^{-1}); f_{d1}, f_{d2} = dissolved fraction of total concentration in each layer ($f_{d1} = f_{d2} = 1$ for NH_4^+, NO_3^- and CH_4); f_{p1}, f_{p2} = particulate fraction of total concentration in each layer $f_{p1} = f_{p2} = 0$ for NH_4^+, NO_3^-, and CH_4); K_{L12} = mass transfer coefficient between layers 1 and 2 ($K_{L12,S}$ is computed specifically for SO_4^{2-} and dissolved H_2S); K_{L01} = ratio of SOD to overlying water dissolved O_2 = mass transfer coefficient between overlying water-column and layer 1; K_{L12} = mass transfer coefficient between layer 1 and 2 (m d^{-1}); ω_2 = sedimentation velocity (m d^{-1}); ω_{12} = particle mixing velocity between layers 1 and 2 (m d^{-1}); k_s = first-order decay coefficient for accumulated benthic stress (d^{-1}); S = benthic stress term (d); J_{T1} = source of solute to layer 1 (mmol m^{-2} d^{-1}); J_{T2} = source of solute to layer 2 (mmol m^{-2} d^{-1}); κ_1, κ_2 = reaction velocity for first-order removal reaction rate constant in layer1 and 2 (m d^{-1}); m_1, m_2 = solids concentration in layer 1 and 2 (kg L^{-1}); π_1, π_2 = partition coefficient in layer 1 and 2 (L kg^{-1}); D_p = diffusion coefficient of particulate solutes due to particle mixing (cm^2 d^{-1}); D_d = diffusion coefficient of dissolved solutes (cm^2 d^{-1}); $\theta_{D_{p,d}}$ = temperature coefficient for D_p or D_d; $K_{M,i}$ = half saturation coefficient (i = relevant parameter or variable, in concentrations units of relevant variable); SOD, CSOD, NSOD = sediment O_2 demand, carbonaceous SOD, and nitrogenous SOD, respectively (mmol O_2 m^{-2} d^{-1}, subscript for CSOD indicates relevant solute); a_{O_2,NH_4} = stoichiometric ratio of O_2 consumed to NH_4^+ oxidized (mol O_2 mol N^{-1}); $a_{O_2,C}$ = Redfield oxygen to carbon stoichiometric coefficient (mol O_2 mol C^{-1}); a_{O_2,NO_3} = stoichiometric ratio for O_2 consumed by denitrification (mol O_2 mol N^{-1}). Where specific solutes are shown (e.g., $[NH_4(i)]$, $[CH_4(i)]$, i = layer). Parameter values listed in Table 2. C_{T1} and C_{T2} were computed for NH_4^+, NO_3^-, ΣH_2S (= dissolved + particulate sulfide), SO_4^{2-}, and $CH_4(aq)$. *$J[CH_4(g)]$ is computed via mass balance of sources and sinks. In the computer code changes in storage are also included in the equation so that the mass balance is exact.

Table 2
Sediment flux model parameters.[§]

Variable	Value	Units	Variable	Value	Units
Recycle fractions			Ammonium		
$f_{POC,N,1}$	0.65		κ_{NH_4}	0.131	m d^{-1}
$f_{POC,2}$	0.20		θ_{NH_4}	1.123	
$f_{PON,2}$	0.25		K_{M,NH_4}	52.0	μM N
$f_{POC,3}$	0.15		θ_{KM,NH_4}	1.125	
$f_{PON,3}$	0.10		K_{M,NH_4,O_2}	11.5	μM O_2
Diagenesis			a_{O_2,NH_4}	2	mol O_2 mol^{-1} N
$k_{POC,N,1}$	0.01–0.035[†]	d^{-1}	Nitrate		
$\theta_{POC,N,1}$	1.10		$\kappa_{NO_3,1}$	0.10–0.30[‡]	m d^{-1}
$k_{POC,N,2}$	0.0018	d^{-1}	$k_{NO_3,2}$	0.25	m d^{-1}
$\theta_{POC,N,2}$	1.15		θ_{NO_3}	1.08	
$a_{O_2,C}$	1.0	mol O_2 mol^{-1} C	a_{O_2,NO_3}	1.25	mol O_2 mol^{-1} N
$a_{N,C}$	0.151	mol N mol^{-1} C	Sulfide		
Solids			$\kappa_{H_2S,d1}$	0.20	m d^{-1}
ω_2	0.25	cm d^{-1}	$\kappa_{H_2S,p1}$	0.40	m d^{-1}
m_1	0.36	kg L^{-1}	θ_{H_2S}	1.08	
m_2	0.36	kg L^{-1}	$\pi_{H_2S,1}$	100	L kg^{-1}
Mixing			$\pi_{H_2S,2}$	100	L kg^{-1}
D_d	5.0	cm^2 d^{-1}	K_{M,H_2S,O_2}	62.5	μM O_2*
θD_d	1.08		K_{M,SO_4}	0.1	μM O_2*
D_p	0.6	cm^2 d^{-1}	D_{SO_4}	1.0	cm^2 d^{-1}
θD_p	1.117		**Methane**		
POC_R	0.1	mg C g solids^{-1}	$\kappa_{CH_4,1}$	0.2	m d^{-1}
$H_1 + H_2$	10.0	cm	θ_{CH_4}	1.08	
Benthic stress			K_{M,CH_4,O_2}	3.125	μM O_2*
k_S	0.03	d^{-1}	CH_{4sat}(STP)	3125	μM O_2*
K_{M,D_p}	62.5	μM O_2*	θ_{CH_4sat}	0.976	

* Indicates that units are in O_2 equivalents.

[†] Diagenesis rate range reflects the new (0.01) and original (0.035) calibration.

[‡] Denitrification reaction velocity range reflects freshwater (0.1) and saltwater (0.3) values used in the original calibration.

[§] See Table 1 for parameter descriptions.

2.8. Particulate organic matter diagenesis and deposition

The above sections address the calculation of sediment flux that results from the deposition of POM to the sediment and the subsequent decomposition of that material (diagenesis) (see Chapter 12 in Di Toro, 2001). Organic matter deposition and diagenesis are modeled by partitioning the settling POM into three reactivity classes (termed the G model by Westrich and Berner, 1984). Each class represents a fixed portion of the organic material that reacts at a specific rate (Burdige, 1991). For SFM, three G classes represent three levels of reactivity: G_1 is rapidly reactive (20 day half-life & 65% of settling POM), G_2 is more slowly reactive (1 year half-life & 20% of settling POM); G_3 (15% of settling POM) is, for this model, non-reactive (diagenesis parameters in Table 2).

Diagenesis of particulate organic carbon (POC) is computed from a mass balance equation and similar equations govern the diagenesis of particulate organic nitrogen:

$$H_2\frac{dPOC_i}{dt} = -k_{POC,i}\theta_{POC,i}^{(T-20)}POC_iH_2 - \omega_2 POC_i + f_{POC,i}J_{POC} \qquad (6)$$

where POC_i is the concentration of POC in reactivity class i in the anaerobic layer, $k_{POC,i}$ is the first order reaction rate coefficient, $\theta_{POC,i}$ is the temperature coefficient, ω_2 is the sedimentation velocity, J_{POC} is the depositional flux of POC from the overlying water to the sediment, and $f_{POC,i}$ is the fraction of J_{POC} that is in the ith G class. The aerobic layer diagenesis is not included because of its small depth relative to the anaerobic layer: $H_1 \approx 0.1$ cm relative to $H_2 \approx 10$ cm. Even if aerobic layer diagenesis was occurring at a more rapid rate (e.g., 10 times faster), the magnitude would be small relative to the anaerobic layer. POM deposition is partitioned into these three classes based on the percentages given above and decomposes at three different rates such that the sediment POM is primarily composed of residual G_3 POM even though it is the smallest portion of settling material.

In order to compute the sediment fluxes of NH_4^+, NO_3^-, and dissolved O_2, the depositional flux of POC (J_{POC}) is required. The strategy adopted in the original calibration of SFM was to estimate the annual flux of PON by fitting the model to the observed NH_4^+ flux (Di Toro, 2001). However, this method ignores the year to year carryover of POM. In fact, adjusting the annual POM deposition to fit NH_4^+ flux over a number of years is a complex estimation problem since every year affects each subsequent year in proportion to the store of organic material that did not undergo diagenesis. A Hooke–Jeeves pattern search algorithm was utilized to minimize the root mean square error (RMSE) between modeled and observed NH_4^+ flux (Hooke and Jeeves, 1961). The pattern search is a method to minimize a cost function – in this application the root mean square error in predicted NH_4^+ flux – by varying parameters, such as the yearly average depositional fluxes. The pattern search starts with an initial estimate of the parameters, in this case a constant yearly organic matter depositional flux of 35 mmol C m^{-2} day^{-1} (a reasonable estimate based on literature derived values (Roden et al., 1995; Kemp et al., 1999, 2007; Hagy et al., 2005)). This is followed by exploratory moves (i.e., ±30%), changing the POM depositional flux for the first year, recording the direction that reduces the current cost function (i.e., NH_4^+ flux RMSE for the first year). This process is repeated for each year and the direction of change (+30% or −30% POM depositional flux) that reduces the error is retained for each year. These directions of change that reduce the RMSE for each year – the pattern – are repeated until the RMSE no longer decreases. The individual year by year search is then repeated and a new pattern is established and repeatedly applied. If it is not possible to find a new pattern, that indicates a local minimum has been found. Then the size of the exploratory moves is reduced from ±30% to ±10% in 10% intervals and finally ±5% to converge to a final solution. The only constraint on depositional flux was a minimum of 8.3 mmol C m^{-2} day^{-1}, 10% below the lowest depositional flux measured in Chesapeake Bay (Roden et al., 1995; Hagy et al., 2005; Kemp et al., 2007).

2.9. Overlying-water concentrations

Data for overlying water-column nutrient and O_2 concentrations nearest the sediment–water interface in Chesapeake Bay, which are required boundary conditions for the stand-alone SFM, were retrieved for each station and date from the Chesapeake Bay Program (CBP) Water Quality database (http://www.chesapeakebay.net/data_waterquality.aspx; see Table 3 for associated CBP sites). Measurements of bottom water salinity, dissolved O_2, ammonium (NH_4^+), and nitrate (NO_3^-) made as part of the Sediment Oxygen and Nutrient Exchange experiments (SONE, Boynton and Bailey, 2008) were augmented by CBP data by combining the time series and using piecewise cubic hermite interpolation (PCHIP) to derive daily overlying water column values. PCHIP is a shape preserving piecewise cubic that spline-interpolates between values but does not exceed the maximum and minimum of the dataset. The fine temporal resolution of the combined SONE and CBP monitoring time series insures that the onset of hypoxia and winter temperature regimes (not measured in the SONE dataset) were properly simulated. To calculate initial sediment nutrient conditions, the time series of POM deposition and overlying water concentrations were repeated until there was 15 years of input. The synthetic 15 year time series was used as the model input, followed by the actual years. This insures that the initial conditions for SFM particulate and dissolved constituents are consistent with the depositional fluxes and parameters.

2.10. Calibration and validation datasets

SFM was calibrated and validated using observational data sets from Chesapeake Bay. Sediment–water fluxes of oxygen (SOD), NH_4^+, and nitrite + nitrate ($NO_2^- + NO_3^-$) were estimated from time-course changes in constituents during incubations of intact plexiglass sediment cores (http://www.gonzo.cbl.umces.edu/sediments.htm, Boynton and Bailey, 2008). In addition to nitrogen and dissolved O_2 fluxes, SONE also provided measurements of surficial sediment chl-*a* (top 1 cm). Average NH_4^+ porewater conditions were validated with measurements made in the top 10 cm of sediment at stations spanning the salinity gradient in Chesapeake Bay from 1971 to 1975 (Bricker et al., 1977). A more recent set of NH_4^+ and NO_3^- porewater measurements in mid-Chesapeake Bay were also utilized (Kemp et al., 1990). Model-data comparisons were facilitated using multiple skill assessment metrics as recommended by Stow et al. (2009): RMSE, mean error (sum of residuals divided by the number of observations), relative error (sum of residuals divided by the sum of observations), correlation (r), and reliability index (RI) were computed for each flux/station combination. Mean error is a measure of aggregate model bias while relative error and RMSE take into account the magnitude of model-data discrepancies. The correlation coefficient (r) measures the tendency of modeled and observed fluxes to vary together. Finally, the RI quantifies the average factor by which model predictions differ from observations. An RI of 2, for instance, would indicate that SFM predicts the observation within a factor 2, on average (Stow et al., 2009).

Table 3
Sediment Oxygen and Nutrient Exchange (SONE) site characteristics. CBP Station represents the Chesapeake Bay Program site designation used for overlying water column data, J_{POC} represents the average depositional flux across all years at each site.

Site	CBP Station	Latitude	Longitude	Depth	SONE years	Salinity	Summer DO	J_{POC}
		°N	°W	m	years		μM O_2	mmol C m^{-2} d^{-1}
Windy Hill	ET5.1	38.8	−75.9	3.3	4.1	1.0	183.1	47.3
Maryland Point	RET2.2	38.4	−77.2	10.1	9.4	1.9	196.8	48.8
Still Pond	CB2.2	39.3	−76.2	10.1	6.5	4.8	167.4	24.6
Horn Point	ET5.2	38.6	−76.1	7.8	16.0	11.1	150.4	34.0
Buena Vista	RET1.1	38.5	−76.7	5.3	17.4	11.5	107.6	45.6
Marsh Point	LE1.1	38.4	−76.6	6.4	13.2	13.2	54.8	42.9
St. Leonard Creek	LE1.2	38.4	−76.5	6.5	17.4	13.6	94.2	29.4
Broome Island	LE1.2	38.4	−76.5	15.2	13.2	13.8	75.7	40.6
Ragged Point	LE2.2	38.2	−76.6	16.4	11.4	15.6	27.5	43.0
R-78	CB3.3C	39.0	−76.4	16.1	4.1	17.0	17.5	19.1
R-64	CB4.3C	38.6	−76.4	16.6	11.3	19.3	14.9	43.3
Point No Point	CB5.2	38.1	−76.2	14.0	11.4	20.6	36.9	27.4

SFM-derived estimates of POM deposition to sediments were validated at station R-64 (Fig. 1) using two previous estimates of deposition: (1) sediment trap measurements made at “mid-water” depths between 1984 and 1992 (7–14 m, Kemp et al., 2007); and (2) modeled deposition based on distributions of “post spring bloom” sediment chl-*a* and kinetics of chl-*a* degradation (Hagy et al., 2005). Overlapping years of chl-*a* degradation based POM deposition and nutrient fluxes were also available for Point No Point. Lastly, model estimates of sulfate reduction were compared to measured rates at stations Still Pond and R-64 (Marvin-DiPasquale and Capone, 1998; Marvin-DiPasquale et al., 2003).

3. Results

3.1. Particulate organic matter deposition

Overall, POM deposition compared favorably with two independent estimates of POM deposition at R-64 (Fig. 5a and b) and Point No Point (Fig. 5c). The mean sediment trap-derived estimate of organic matter deposition at R-64 from 1984 to 1992 was 46.7 mmol C m^{-2} day^{-1} compared to the model estimate of 43.7 mmol C m^{-2} day^{-1} (6.4% lower; Fig. 5a). POM deposition estimated from sediment chl-*a* distributions at R-64 from 1993 to 1996 was 35.7 mmol C m^{-2} day^{-1} compared to the model estimate of 38.9 mmol C m^{-2} day^{-1} (8.9% higher; Fig. 5b). Similar estimates obtained downstream of this site at Point No Point were 31.7 mmol C m^{-2} day^{-1} compared to model estimates of 24.6 mmol C m^{-2} day^{-1} (Fig. 5c).

Across all stations the range of POM deposition was 19.3 mmol C m^{-2} day^{-1} at R-78 to 48.3 mmol C m^{-2} day^{-1} at Maryland Point (Table 3). Spatial patterns in the mainstem of Chesapeake Bay were also consistent with sediment chl-*a* distributions in Hagy et al. (2005). POM deposition increased from 24.0 mmol C m^{-2} day^{-1} at Still Pond (275 km from the mouth of the bay) to 43.3 mmol C m^{-2} day^{-1} at R-64 (192 km from the mouth of the bay) and the decreased to 26.0 mmol C m^{-2} day^{-1} down bay at Point No Point (130 km from the mouth of the bay) (Table 3).

Although overall fits to average POM deposition were encouraging, there were substantial differences in interannual variability. This was especially apparent in a comparison of model and sediment trap-derived estimates, where six out of nine years of modeled POM deposition fell outside the range of the data (Fig. 4a; Roden et al., 1995). In contrast, in six out of eight years, the modeled POM deposition fell within the range of the observations for the sediment chl-*a* distribution estimates (Fig. 4b and c; Hagy et al., 2005). Differences between modeled and observed POM deposition were especially pronounced following years of high modeled deposition. For example, in 1987, the year after the highest modeled POM deposition at R-64 (Fig. 5a), the sediment trap-derived estimate for POM deposition was 45.3 mmol C m^{-2} day^{-1}, whereas the modeled estimate was 8.3 mmol C m^{-2} day^{-1} (Fig. 5a). Interannual variability of model estimates was much more closely aligned with interannual variability in sediment chl-*a* distribution estimates. The standard deviation around annual POM deposition estimates was 2.75 mmol C m^{-2} day^{-1} for the sediment trap derived estimates, 15.0 mmol C m^{-2} day^{-1} for sediment chl-*a* distribution estimates, and 18.4 mmol C m^{-2} day^{-1} for model estimates.

Further validation of modeled POM depositional flux is available in the comparison of observed sediment chl-*a* with modeled G_1 carbon in the sediment (e.g., Station R-64, Fig. 6). Sediment chl-*a* was converted to G_1 carbon using a commonly applied carbon to chl-*a* ratio in the Chesapeake Bay of 75 C:CHL and assuming that all chl-*a*-based carbon was G_1. A strong correlation was observed at most sites ($r = 0.6$) indicating that carbon delivery and

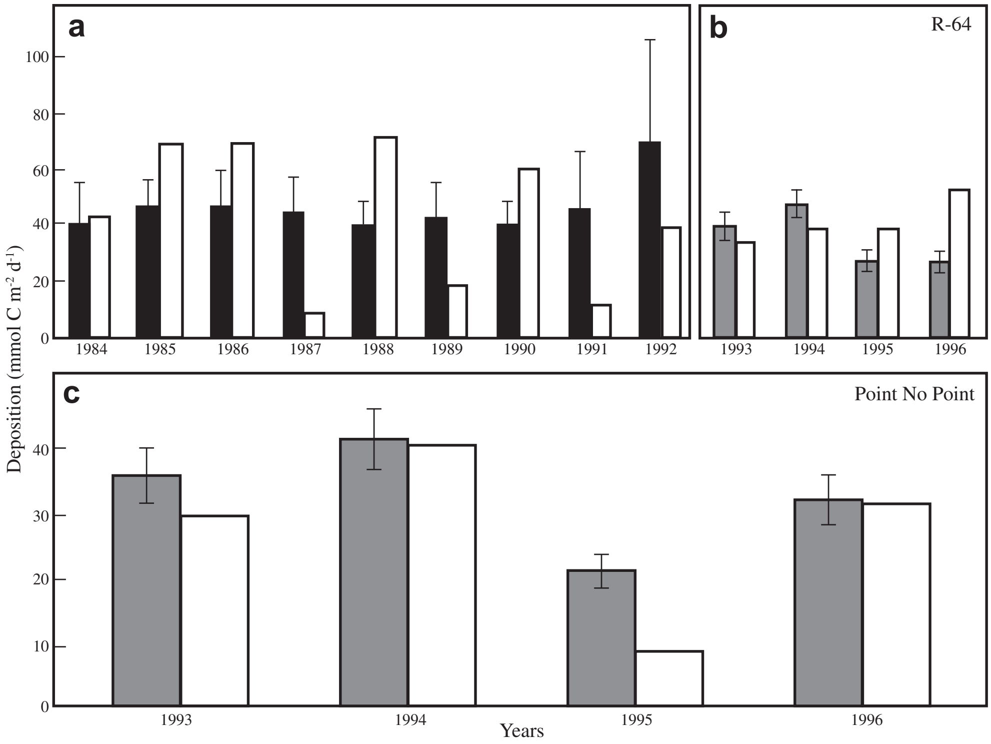

Fig. 5. Time series of annual averages for observed (black and gray) and modeled (white) particulate organic carbon deposition to sediments for two Chesapeake Bay stations (R-64 and Point No Point). Panel a observations (black) were measured using sediment traps (Kemp et al., 2007; Roden et al., 1995). Gray bars (Panels b & c) are for observations computed using sediment chlorophyll-*a* measurements (Hagy et al., 2005). Model estimates represent output using a carbon diagenesis rate of 0.01 day^{-1} and time invariant deposition within each year.

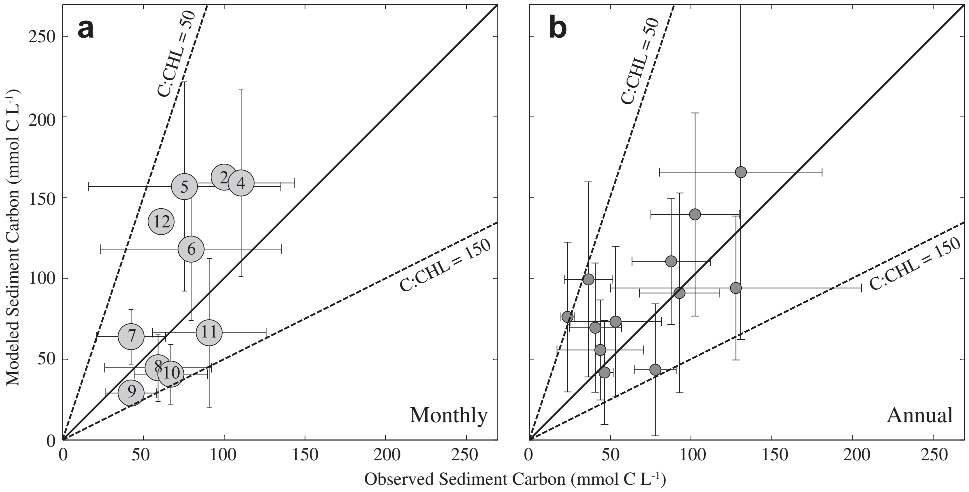

Fig. 6. Monthly (left panel, a) and annual (right panel, b) comparisons of observed and modeled sediment organic carbon at Station R-64 (concentrations in mmol per liter of sediment solids). Modeled sediment organic carbon is the G_1 fraction (calculated by assuming a solids concentration of 2.6 g cm^{-3}; Di Toro, 2001 Chapter 1), while observed sediment organic carbon is estimated from measured sediment chlorophyll-*a* converted to carbon using a carbon:chlorophyll-*a* (C:CHL) ratio of 75. Model and observation data are represented by circles and are means across all stations, while 1:1 lines for a C:CHLA of 50 and 150 are dashed lines. Solid line is 1:1 line for C:CHL of 75.

decomposition were well simulated. Even sites with poor correlations were well within the observed range of carbon to chl-*a* ratios in the Bay (Hagy et al., 2005; 50–150 C:CHL; Fig. 5). Therefore, poor correlation between surficial chl-*a* and modeled G_1 carbon may have more to do with variability in carbon to chl-*a* ratios than incorrect simulation of carbon delivery. For example, monthly ($r = 0.65$) and annual ($r = 0.63$) comparisons of sediment carbon from R-64 are shown in Fig. 6a and b, respectively. In comparisons made on a monthly basis, late spring/early summer months (April–June) clustered close to the low carbon to chl-*a* ratio (50 C:CHL) and late summer-fall months (August–October) tended to cluster around the high carbon to chl-*a* ratio. This clustering pattern was consistent across sites and indicates that the C:CHL ratio of deposited material varies seasonally (Malone et al., 1988).

3.2. *Validating ammonium flux*

The sequence of annual average POM deposition estimated using the Hooke Jeeves algorithm resulted in good fits between modeled and observed interannual temporal variation of NH_4^+ flux (Fig. 7). All sites had low RMSE and little bias in mean error (Table 4). Modeled NH_4^+ flux at a relatively oxic site that tends toward denitrification (Still Pond; Table 3) was 57.7 μmol m^{-2} h^{-1} compared to an observed flux of 55.5 μmol m^{-2} h^{-1} (Fig. 7). A more hypoxic site such as Buena Vista had an average modeled NH_4^+ flux of 360 μmol m^{-2} h^{-1} compared to an observed average NH_4^+ flux of 364 μmol m^{-2} h^{-1} (Fig. 7).

The model also successfully simulates the seasonal shift from NH_4^+ accumulation to NH_4^+ flux. During winter months, NH_4^+ builds up in the anaerobic layer of sediment and the production of NH_4^+ from diagenesis (J_N) exceeds the efflux of NH_4^+ lost to the overlying water. Although the concentration gradient between the overlying water and the anaerobic layer would indicate efflux should occur, surface mass transfer is very low during this period (data not shown). During summer months, the magnitude of the fluxes reverses and the store of NH_4^+ in the anaerobic layer is depleted by NH_4^+ flux to the overlying water. Matching this intra-annual signal in NH_4^+ flux is strongly dependent on the presumed intra-annual variability in deposition and model parameterization.

One method of testing the former was to presume that POM deposition is related to the seasonal variability in surface chl-*a*. Organic matter depositional flux based on the seasonal pattern in surface chl-*a* and particulate matter sinking velocities (Kemp et al., 2007) resulted in a relatively poor overall correlation coefficient of $r = 0.53$ on a monthly basis (Figs. 8a, d and g). Monthly modeled spring-summer NH_4^+ fluxes were universally overestimated and fall-winter NH_4^+ fluxes were underestimated. Model estimates were improved by assuming a constant annual depositional flux which resulted in an increase in correlation to $r = 0.70$ (Figs. 8b, e and h). Using this formulation for POM deposition, spring-summer overestimation and fall-winter underestimation were reduced but not completely eliminated. This was the formulation employed in the original SFM calibration (Di Toro, 2001). The assumption of constant annual deposition is supported by sediment trap estimates, made at station R-64 from 1984 to 1992, that show a weak bimodal seasonal distribution (Kemp and Boynton, 1992; Kemp et al., 1999) with significant month to month variability (Roden et al., 1995; Kemp et al., 2007).

The combination of annually constant organic matter deposition and a reduction in the POM diagenesis rate constant ($k_{POC,N,1}$ in Table 2) from 0.03 day^{-1} to 0.01 day^{-1} resulted in a much stronger monthly correlation ($r = 0.86$) across all sites (Figs. 8c, f and i). As shown in Fig. 8, this modification shifted the peak in NH_4^+ flux from June–July as in the original calibration (gray lines) to July–August (black lines; Fig. 8) and improved the model's skill at simulating high summer NH_4^+ fluxes by increasing the pool of available G_1 nitrogen available for depletion during the warmer months. The slower diagenesis rate (0.01 day^{-1}) compared to the original calibration (0.03 day^{-1}) improved model-data fits at every site. For example, the monthly correlation coefficient between modeled and observed NH_4^+ flux at St. Leonard's Creek improved from 0.32 assuming a surface chl-*a* derived seasonal signal and faster diagenesis to 0.96 assuming a constant depositional flux and slower diagenesis rate.

High mid-to-late summer NH_4^+ flux is not the result of the gradient between overlying water column NH_4^+ and anaerobic layer porewater concentrations. In fact, periods of high NH_4^+ flux correspond to periods of low modeled concentration gradients. Instead, high fluxes result from model parameterization of mixing. Summer periods of high SOD and low overlying water O_2 (Fig. 10) serve to increase the surface mass transfer coefficient and therefore produce relatively high fluxes. Nonetheless, model

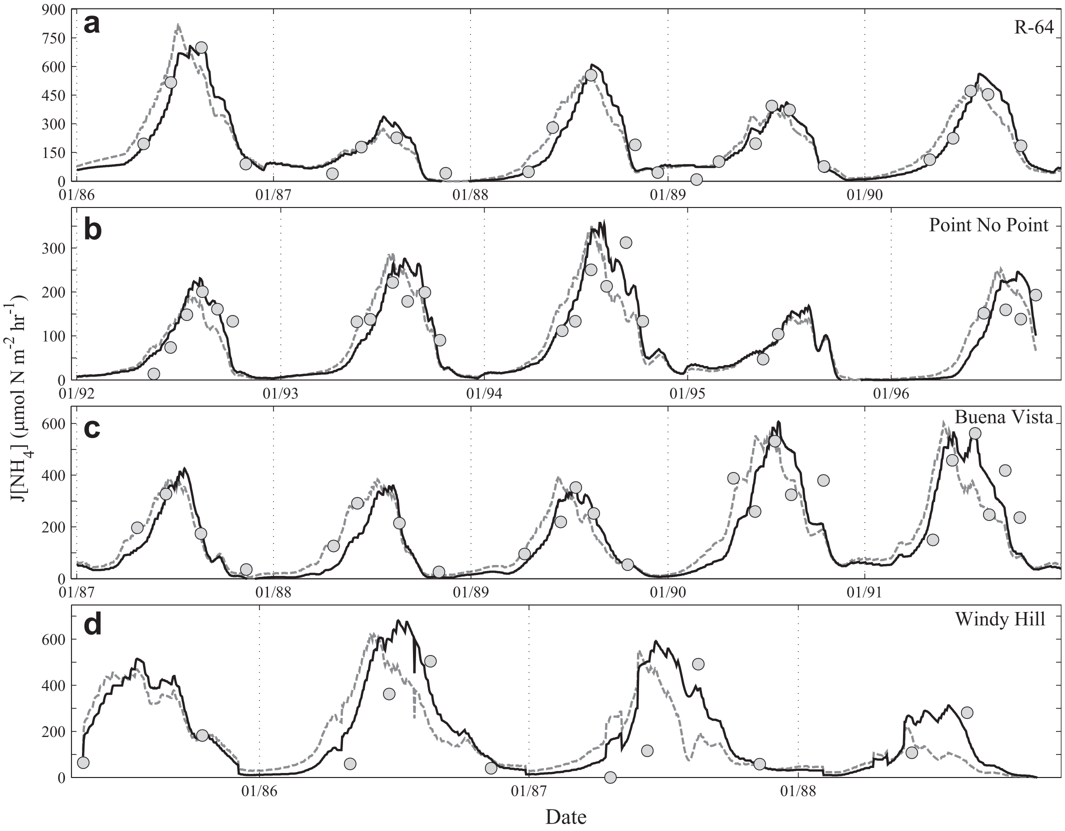

Fig. 7. Modeled (lines) and observed (circles) time series of NH_4^+ flux from four stations in Chesapeake Bay (a: R-64, b: Point No Point, c: Buena Vista, d: Windy Hill). Gray dashed lines represent model output using the diagenesis rate (k_{POC}) of 0.03 day^{-1} from the original calibration and black solid lines represent model output using a diagenesis rate of 0.01 day^{-1}.

computations of porewater concentration are a check on model parameterization of mixing. Fig. 9 presents a comparison of the model anaerobic layer NH_4^+ concentrations and observed (0–10 cm) porewater concentrations. Although model-data comparisons do not overlap in time (i.e., data represent average porewater NH_4^+ concentrations during the late 1970s and model output represents the mid 1980s to mid 1990s), modeled porewater concentrations along the mainstem of the bay are within the variability of the observed porewater concentrations. Model-data comparisons of porewater NH_4^+ also improved when the diagenesis rate of G_1 POM was decreased.

Table 4
Root mean square error (RMSE), mean error (ME), relative error (RE), and correlation coefficient (r) for model-data comparison of NH_4^+ flux and sediment oxygen demand (SOD).

Sites	J[NH4] (μmol N m^{-2} h^{-1})				SOD (mmol m^{-2} day^{-1})			
	RMSE	ME	RE (%)	r	RMSE	ME	RE (%)	r
Windy Hill	151.1	−50.03	67.4	0.65	29.0	15.4	34.1	0.38
Maryland Point	144.1	−20.27	66.0	0.57	16.0	−5.3	39.5	0.62
Still Pond	71.4	−1.89	78.8	0.54	15.5	4.6	40.9	0.46
Horn Point	116.0	−4.42	30.4	0.69	17.0	0.6	39.3	0.64
Buena Vista	105.5	3.92	26.8	0.78	24.4	10.9	31.8	0.40
Marsh Point	72.3	2.24	35.5	0.75	30.0	14.8	44.0	0.29
St. Leonard Creek	93.6	6.90	27.2	0.67	15.9	−2.3	37.7	0.39
Broome Island	78.3	4.89	44.9	0.59	13.1	1.9	43.4	0.47
Ragged Point	66.0	−1.02	29.0	0.80	28.3	16.9	44.5	0.27
R-78	85.8	35.57	65.7	0.48	11.8	6.0	56.5	0.41
R-64	92.8	−1.94	29.0	0.81	15.4	−2.9	64.4	0.53
Point No Point	113.0	−0.43	37.5	0.73	18.1	−3.3	75.0	0.49

Anaerobic layer NH_4^+ concentrations were used in the original calibration (Di Toro, 2001) to calibrate the diffusive mass transfer coefficient between the anaerobic and aerobic layers (K_{L12}). Although observed porewater concentrations do not cover the same time period, there is general agreement between modeled and observed concentrations. In fact, across all years and sites observed anaerobic NH_4^+ porewater concentrations were 712.8 μM whereas modeled porewater concentrations were 649.7 μM (Fig. 9, 8% lower than observed). Additionally, in the original calibration the computed intraannual peak in NH_4^+ concentration occurred in May, while observed NH_4^+ concentrations peak in August. Using a lower diagenesis rate for G_1 carbon in the updated calibration ameliorated the phase difference between the peak in observed (August) and modeled (July) porewater NH_4^+.

3.3. Sediment oxygen demand

The metabolic activity of sediments (i.e., respiration of organic matter) is often estimated using sediment O_2 demand (SOD) (Cowan and Boynton, 1996). When the water-column overlying deep-water sediments in estuaries like Chesapeake Bay becomes anaerobic, SOD goes to zero. The components of modeled SOD that can be directly compared to SOD observations include the oxidation of sulfide, methane, and NH_4^+ generated by carbon diagenesis.

Comparisons of observed SOD with model predictions provides an independent validation of POM deposition and NH_4^+ flux estimates. Fig. 10 presents model-data comparisons for two oxic stations and two stations where overlying water O_2 concentrations, shown in gray shading, is zero for periods of time. In our analysis, model SOD estimates compared favorably with observations

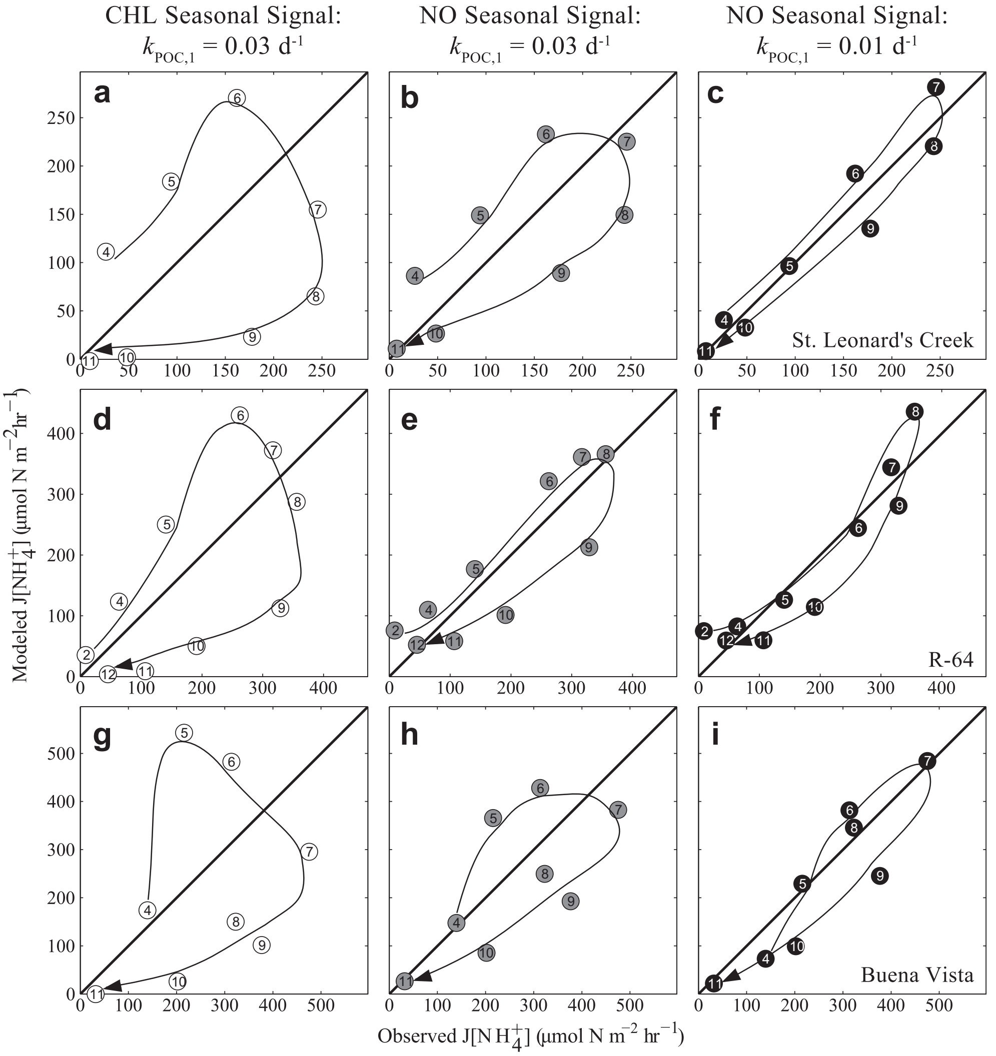

Fig. 8. Modeled versus observed monthly NH_4^+ fluxes at three stations in Chesapeake Bay (St. Leonard's Creek (a, b, c), R-64 (d, e, f), Buena Vista (g, h, i)) using three different estimates of organic matter deposition: (left to right) seasonally varying deposition based on overlying water column chlorophyll-*a* (a, d, g), annual average deposition (i.e. constant deposition) with the original calibration diagenesis rate of 0.03 day^{-1} (b, e, h), and annual average deposition with a diagenesis rate of 0.01 day^{-1} (c, f, i).

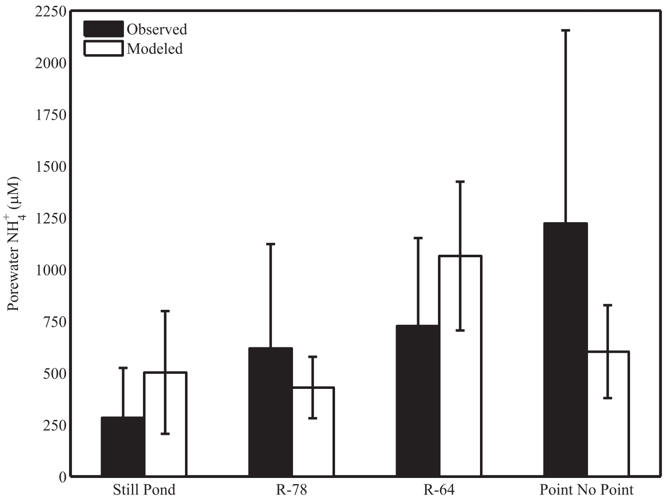

Fig. 9. Modeled (black) and observed (white) average (±SD) porewater NH_4^+ concentrations at four stations along the main axis of Chesapeake Bay. Observations are average of measurements made within the top 10 cm of sediment cores collected in 1973–1975 (Bricker et al., 1977) and 1986 (Kemp et al. 1990).

seasonally during several years at multiple stations with an overall RMSE less than 20 mmol O_2 m^{-2} day^{-1} (Table 4). The model captured differences in seasonal SOD cycles among sites with varying levels of overlying-water O_2. At stations where hypoxic conditions did not develop (Horn Point, Maryland Point; Fig. 10a and b), SOD increased during warmer months and generally followed the seasonal temperature cycle. Conversely, at sites with seasonal hypoxia and anoxia (R-64, Ragged Point, Figs. 10c and d), SOD increased through spring, but declined precipitously in early summer when O_2 concentrations rapidly declined to concentrations below 62.5 μM (Fig. 10c and d). At such sites, SOD episodically increased when overlying-water O_2 concentrations recovered from hypoxia (Fig. 10c and d).

Comparisons of CSOD and NSOD with the sediment–water fluxes of reduced species under anaerobic conditions allows for a comparison of reduced species between sites. Fig. 11 presents the CSOD and NSOD components of SOD, and the fluxes of sulfide and methane to the overlying water computed by the model. At R-64, a deep, seasonally-anoxic site in mid-Chesapeake Bay, CSOD and NSOD dominate SOD in winter and fall, with CSOD as the primary contributor to SOD (Fig. 11). However, during anoxic summer months, sediment–water sulfide fluxes dominate, revealing

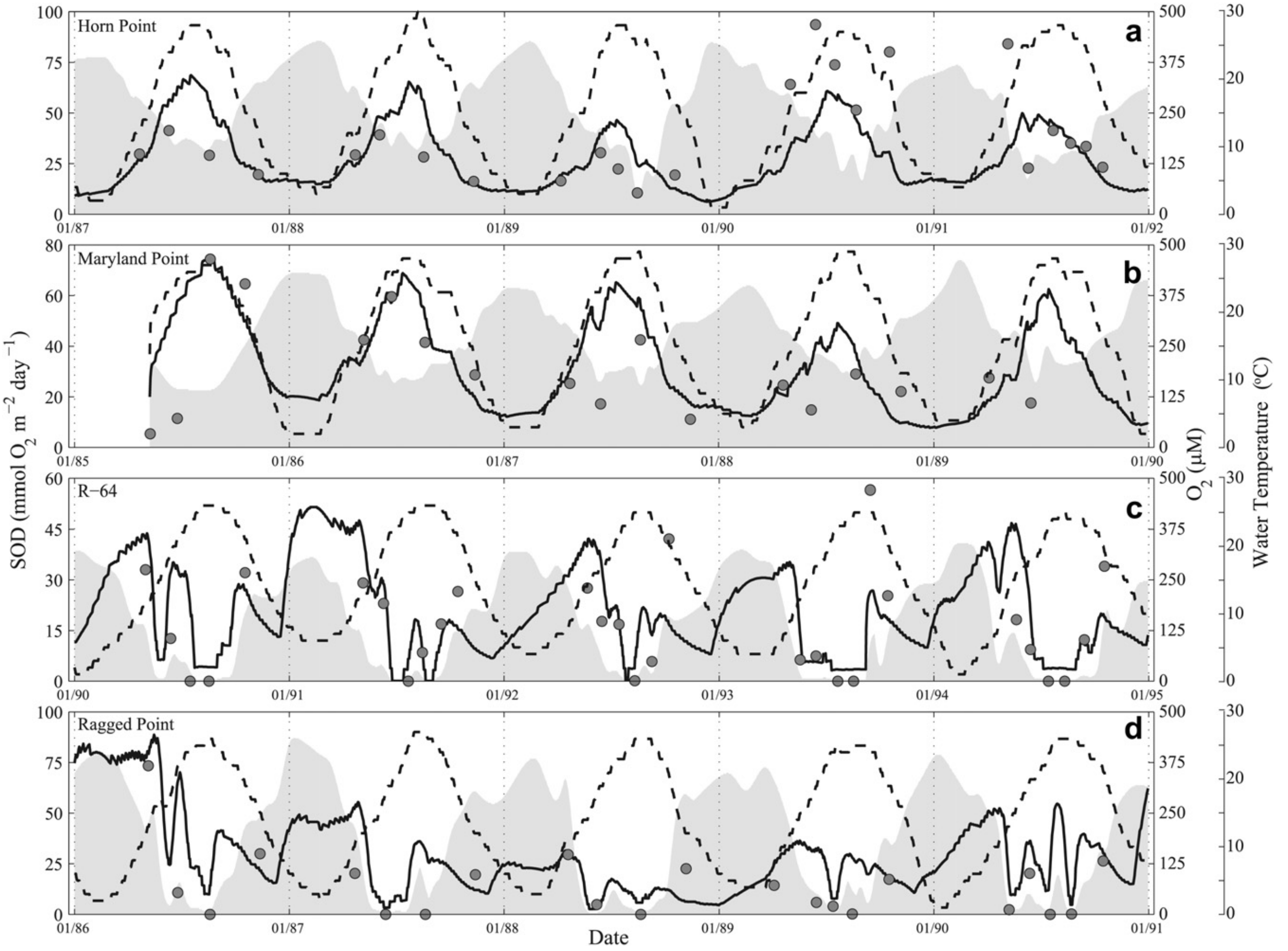

Fig. 10. Modeled (lines) times series of nitrogenous plus carbonaceous sediment oxygen demand (SOD) and observed (circles) SOD at four stations in Chesapeake Bay (a: Horn Point, b: Maryland Point, c: R-64, d: Ragged Point). Gray area plot represents overlying water column dissolved oxygen and dashed line represents water temperature.

sediment efflux of accumulated reduced sulfur (Fig. 11). In contrast, SOD reaches peak rates in summer months at Still Pond, in the more oxygenated upper-Bay, and sediment–water CH_4 fluxes (aqueous and gaseous) contribute 30–50% of the O_2 equivalents within these relatively low-salinity (i.e., low-SO_4^{2-}) sediments.

Model simulations of the sulfur system (and of diagenesis) can be further validated by comparing modeled rates of sulfate reduction to observations made in Chesapeake Bay in the 1990s (Marvin-DiPasquale and Capone, 1998). As shown in Fig. 12, model-field data comparisons correlate seasonally at R-64 and Still Pond, where rates generally peak during the summer period at both stations. Observations and model computations are also comparable in magnitude at Still Pond, although observed rates were generally higher than model predictions at R-64 (Fig. 12). Sulfate reduction rates were always higher at R-64. Interestingly, modeled *and* observed sulfate reduction rates decreased in mid-summer at Still Pond in 1989, but not in later years (Fig. 12).

4. Discussion

4.1. POM deposition

SFM provides a framework within which to analyze measured nutrient and O_2 fluxes and to see if they either contain surprises or conform to previous observational relationships. Additional benefits are estimates of POM deposition to sediments which are perhaps the most unique products of stand-alone SFM simulations. Because of the effort and complications associated with sediment trap deployments and other techniques for estimating POM deposition, SFM provides a useful process-based, observation-driven quantitative tool to make such estimations. Coupling between pelagic and benthic habitats is a fundamental feature of most shallow coastal aquatic ecosystems (Nixon, 1981; Kamp-Nielsen, 1992; Kemp and Boynton, 1992; Soetaert and Middelburg, 2009), and POM deposition is the primary link of the water-column and sediments. Just how sediments respond to variations in POM deposition is a perpetually important question for the understanding and management of estuarine processes, as is quantification of the response magnitude and time-scale of sediment–nutrient fluxes in response to reduced POM deposition (see Chapter 16 in Di Toro, 2001).

Our comparisons between SFM estimates of POM deposition and those computed from two independent methods reveal several key characteristics of POM transport in Chesapeake Bay. POM deposition estimates based upon post-spring-bloom sediment chl-*a* distributions (Hagy et al., 2005) compare more favorably with SFM calculations on an interannual basis than did estimates from sediment traps (Kemp et al., 2007). Both SFM estimates and chl-*a* distributions (Hagy et al., 2005) use indicators of deposition that are based on sediment processes. Sediment traps, on the other

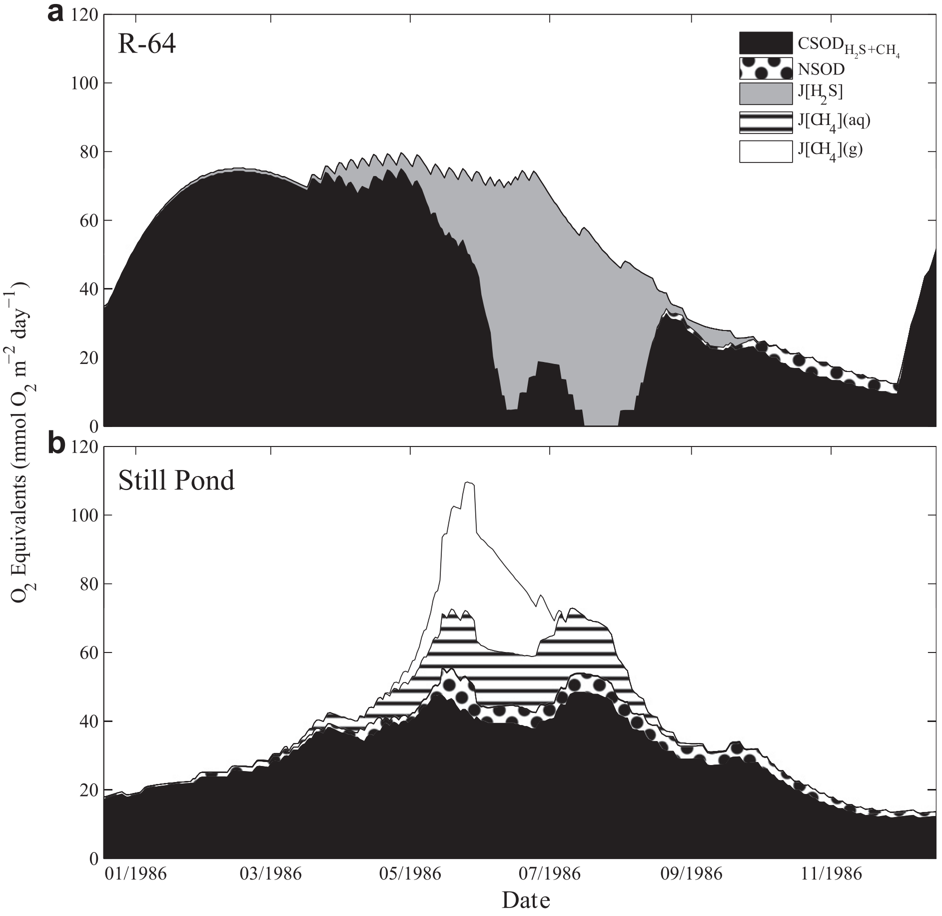

Fig. 11. Modeled seasonal cycle of SOD components and sediment–water fluxes of reduced solutes (in O_2 equivalents) at stations R-64 (top panel, a) and Still Pond (bottom panel, b) for 1986. CSOD is carbonaceous SOD (black), NSOD is SOD due to nitrification (black dots), $J[H_2S]$ is the sediment–water sulfide flux (gray), and $J[CH_4](aq)$ (horizontal black lines) and $J[CH_4](g)$ (white) represent sediment–water fluxes of aqueous and gaseous methane, respectively.

hand, were deployed at mid-water-column depths (8–14 m). Material captured in the traps include resuspended material from adjacent shallow-shoals in Chesapeake Bay (Kemp and Boynton, 1984). Also, a fraction of the material crossing the pycnocline may not reach the sediment, as it may be respired or advected to other regions after passing the sediment trap.

A secondary validation of SFM estimates for POM deposition involves correlations between modeled pools of labile organic carbon in sediments (G_1) and observed surface-sediment chl-*a*. Correspondence between chl-*a* accumulations in sediment, an index of recent POM deposition, and elevated accumulations of labile carbon provides evidence that both POM deposition rates and diagenesis rates are well-constrained. However, seasonal changes in the relationship between sediment chl-*a* and G_1 carbon also indicate that the carbon to chl-a ratio (C:CHL) of deposited POM changes seasonally. As shown in Fig. 6, in spring and winter months, the C:CHL ratio is closer to that of diatom communities (<75), while summer and autumn C:CHL is closer to smaller-celled species (>75) (Malone et al., 1988).

4.2. Diagenesis

The parameter optimization routine was also used to compute the rate of decomposition of the various organic matter fractions delivered via POM deposition. The original calibration of SFM used a first-order decomposition rate constant of G_1 carbon of 0.035 d^{-1} (Di Toro, 2001). As a result, NH_4^+ fluxes increased rapidly in spring, resulting in the over prediction of NH_4^+ fluxes in April–June, and the underestimation of these fluxes in August–October (Figs. 7 and 8). Optimizations of this decomposition rate over all stations in Chesapeake Bay resulted in a slower rate constant ($k_{POC,1} = 0.01\ d^{-1}$) than previously used for G_1 carbon pool, and the seasonal mismatch of modeled and observed NH_4^+ fluxes disappeared with the latter parameter value (Figs. 7 and 8). In fact, this slower rate constant is consistent with available measurements in Chesapeake Bay (0.01–0.023 d^{-1}, Burdige, 1991), though less than other rates reported for marine systems (0.02–0.03 d^{-1}, Westrich and Berner, 1984; Roden and Tuttle, 1996). One important consequence of this reduced rate is that G_1 carbon may be retained in the sediments late into the season and into subsequent years.

One of the central questions for nutrient management is: how long will it take for ecosystem properties (e.g., chl-*a*, POM deposition, nutrient recycling) to respond to reduced nutrient loading? From this perspective, the time variable behavior of SFM can be used as a tool to estimate the legacy of eutrophication as measured by residual oxidizing material that remains in the sediment even after remediation. An excellent example can be seen during 1987 (Fig. 5a at R-64). The second highest POM deposition estimate on record at R-64 was in 1986. Subsequently, due to low NH_4^+ fluxes observed in 1987, POM deposition was minimal that year. However, at the end of 1987 there was still 20% and 65% of the G_1 and G_2

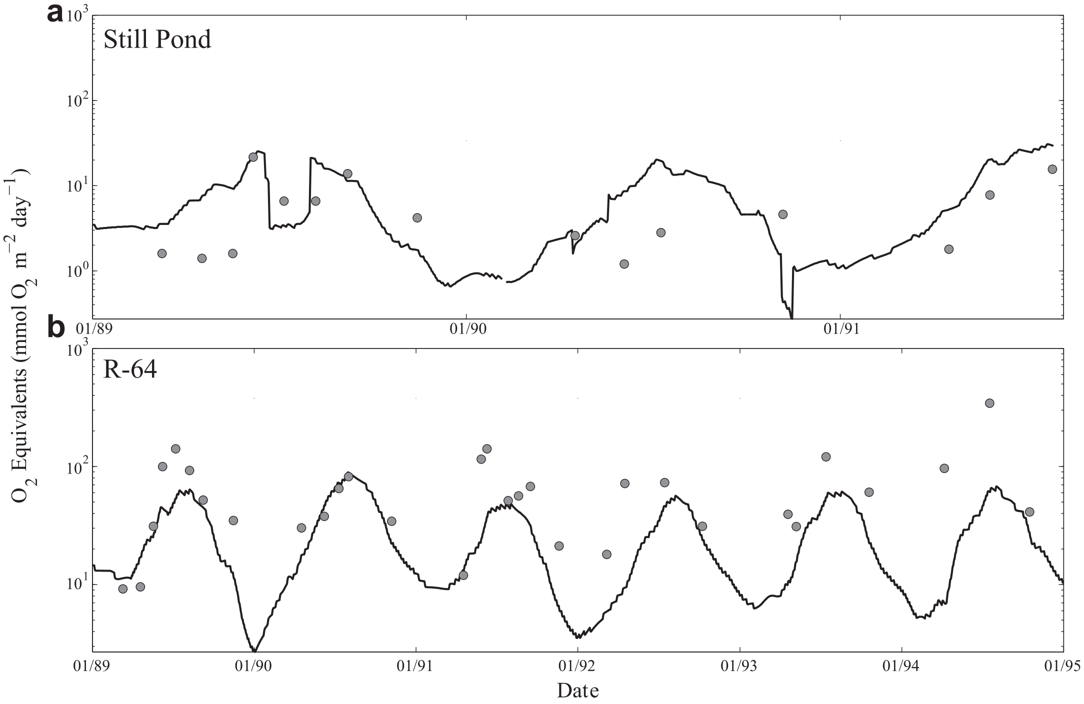

Fig. 12. Time series of observed (circles) and modeled (line) sulfate reduction rates at Still Pond (top panel, a) and R-64 (bottom panel, b). Sulfate reduction was measurements were made by Marvin-DiPasquale and Capone (1998).

carbon deposited during 1986 remaining in the sediment. This result indicates that high deposition in 1986 continued to influence NH_4^+ fluxes in subsequent years. Minor parameter changes in the diagenesis rate of the G_2 portion of organic material can magnify the latent effects of high POM deposition.

4.3. SOD

Seasonal cycles of SOD at stations where the overlying water-column is oxic and hypoxic are out of phase with one another, illustrating the switch between aerobic and anaerobic respiration. SOD time courses exhibit summer peaks at stations where overlying-water O_2 levels remain above 62.5 mM for the majority of the year (Fig. 10); this clearly reflects temperature-driven, aerobic respiration and oxidation of reduced metabolites, where SOD is unlimited by O_2 availability. Conversely, SOD is generally depressed in summer months and higher in spring at stations characterized by summer anoxia and hypoxia (Fig. 10). Strong O_2-limitation of SOD occurs at these stations, which is further illustrated by occasional, short-lived SOD peaks during summer when O_2 concentrations are slightly elevated (Fig. 10). Observational methods used to measure SOD can only measure O_2-uptake, thus anaerobic metabolism cannot be observed directly. Similarly, modeled SOD rates only represent terms in the SOD equation that involve O_2 uptake, thus the generation and subsequent storage or efflux of reduced metabolites under anaerobic conditions is not represented by modeled SOD. Indeed, relatively high modeled SOD in the first months of the year reveals the oxidation of reduced sulfide stored during anaerobic periods of the previous year (Fig. 10).

The phenomenon of winter/early spring SOD highlights the potential for delayed oxidation of reduced sulfur in SFM. SFM apportions the end productions of carbon diagenesis via sulfate reduction into 3 pathways: (1) the oxidation of dissolved and solid-phase sulfide, the diffusion of sulfide to the overlying water, and the burial of solid-phase sulfide. At stations with seasonally anaerobic overlying water, dissolved sulfide accumulates during summer and cannot be oxidized in sediments, resulting in modeled sediment–water fluxes of sulfide (J[H_2S]; Fig. 11, R-64). Sulfide remaining in sediment (both H_2S and FeS), which was not buried or diffused to overlying water under anoxic conditions, will be gradually oxidized as it is mixed into the aerobic layer in later periods. This is evident at R-64 from December through February as SOD increases (Fig. 11).

Validation of these sulfur dynamics can be approached by considering the correspondence between modeled and measured sulfate reduction rates (Marvin-DiPasquale and Capone, 1998) (Fig. 12). At stations where low SO_4^{2-} concentrations may limit sulfate reduction, methane formation occurs in the anaerobic layer. Although dissolved methane diffuses into the aerobic layer and is oxidized to CO_2, serving as an O_2 sink, in summer at the more freshwater sites in Chesapeake Bay, sediment water fluxes of both dissolved methane and methane gas occur. At times when sediment–water methane fluxes are nearly equivalent to SOD, as in June of 1986 at Still Pond (Fig. 11), sediment metabolism would be highly underestimated if SOD was used as the only metric of diagenesis. In fact, a measured and modeled decline in mid-summer sulfate reduction at Still Pond in 1989 (Fig. 12) corresponds to a period of very high river flow from the Susquehanna River (data not shown). As a result of the high river flow, freshwater conditions prevailed at this station, limiting sulfate reduction. Model simulations indicated that diagenesis during this period did not slow, as methanogenesis rates peaked, resulting in relatively high rates of SOD_{CH_4} and sediment–water gaseous CH_4 fluxes. Thus, SFM in this case provided a mechanistic interpretation of sediment dynamics that would not have been realized from observations alone.

The weighted (i.e., by years of observations in Table 3) mean error across all sites in SOD is relatively small (2.7 mmol O_2 m^{-2} day^{-1}) and the reliability index of 1.34 indicates that the model simulates SOD quite well and is not biased. However, there are several years, such as 1990 at Horn Point (Fig. 9), where high SOD residuals suggest that the relationship between

NH_4^+ flux and POM deposition flux is inadequate to predict SOD. As shown in Fig. 13, this was particularly true for years following high nutrient loads at stations near the head of tide. Because these stations are near the source of terrestrially-derived nutrient and carbon loading, it is reasonable to assume that POM deposition at these sites may have a relatively higher C:N ratio (Burdige and Zheng, 1998) than the Redfield ratio used in the model. If this is the case, the high correlation between SOD residuals and the previous year's TN loading suggests that pulsed loading may result in a surplus of G_2 carbon that consumes more O_2 than expected in subsequent years based on within year POM deposition as deduced from the NH_4^+ flux.

4.4. Missing nitrogen processes

It should be noted that other nitrogen cycling pathways, namely, anaerobic NH_4^+ oxidation (anammox), dissimilatory nitrate reduction to ammonium (DNRA), and nitrogen fixation (Buring and Hamilton, 2007), the importance of which has recently been recognized, are not currently simulated in SFM. Anammox is defined as the oxidation of NH_4^+ with nitrite (NO_2^-) in the absence of O_2 ($NH_4^+ + NO_2^- \rightarrow N_2 + H_2O$). Anammox was first discovered in a wastewater treatment systems (Mulder et al., 1995) but has since been observed in Chesapeake Bay (Tal et al., 2005). However, N_2 production as a result of anammox was generally confined to the freshwater tidal portion of the bay and ranged from 0 to 22% of the N_2 production (Rich et al., 2008). Nonetheless, current model formulations require a close coupling of nitrification-denitrification for nitrogen removal and explicit inclusion of anammox would change the dynamics of N_2 production when these systems are decoupled in freshwater tidal areas of the bay. DNRA is another form of anaerobic respiration wherein NO_3^- is reduced to NH_4^+ thereby keeping available nitrogen in the system (Gardner et al., 2006). DNRA has not been measured in Chesapeake Bay. However; Gardner et al. (2006) and Koop-Jakobsen and Giblin (2010) found that DNRA was a major source of NH_4^+ production and on par with denitrification rates in anoxic sediments in Texas and Massachusetts estuaries, respectively. Currently, rates of DNRA would be subsumed in the SFM denitrification rate formulation (but without generating NH_4^+), which implies that NO_3^- loss terms could be underestimated in the model during conditions favorable for DNRA (e.g., high sulfide; Gardner et al., 2006). Finally, nitrogen fixation has been observed at significant levels in some estuaries (Fulweiler et al., 2007), although seldom observed in Chesapeake Bay (Marsho et al., 1975). If nitrogen fixation is a significant source of NH_4^+ it could readily be incorporated into SFM.

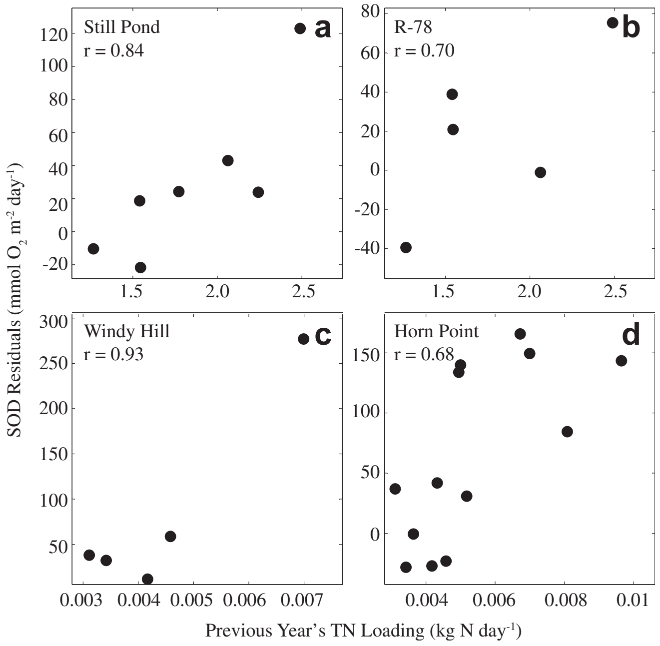

Fig. 13. Annual average sediment oxygen demand (SOD) residuals (observed-predicted) correlated with the previous year's annual average total nitrogen (TN) loading from the Susquehanna (stations: (a) Still Pond and (b) R-78) and Choptank (Stations: (c) Windy Hill and (d) Horn Point) Rivers.

4.5. Model application, improvement, and implementation in other systems

The applicability of SFM in a wide-variety of habitats has been demonstrated via its successful integration into water quality models in many coastal systems, including Massachusetts Bay (Jiang and Zhou, 2008), Chesapeake Bay (Cerco and Cole, 1993; Cerco, 1995; Cerco and Noel, 2005), Delaware's Inland Bays (Cerco and Seitzinger, 1997), and Long Island Sound (Di Toro, 2001) and Marine Ecosystem Research Laboratory (MERL) mesocosms (Di Toro and Fitzpatrick, 1993; Di Toro, 2001). SFM is also currently coupled to a number of commonly-used water-quality platforms, including CE-QUAL-ICM (Cerco and Noel, 2005), WASP (http://www.epa.gov/athens/wwqtsc/html/wasp.html), and RCA (Fitzpatrick, 2009). SFM performed well in a wide-ranging set of conditions in Chesapeake Bay, covering large gradients in salinity, O_2, nutrients, and POC deposition.

The stand alone SFM can be utilized to answer many questions given its rapid execution times and previous application to several different coastal systems. For example, SFM can be used to explore the interactions of POM deposition and water-column O_2 levels on SOD and nitrogen and phosphorus cycling (e.g., nitrogen recycling efficiency) and their feedback effects on water-column phytoplankton growth. Sediments have also been said to be responsible for retaining nutrients and thus storing a "memory" of eutrophication that forces time lags between management actions and ecosystem response, and SFM can be used to explore these lags over long time-periods.

There are several limitations of SFM that could be improved in the future. First, model estimates of POM deposition require application of observed sediment–water NH_4^+ fluxes, which can be costly to obtain, and this may limit the potential for running prognostic scenario analysis. Our preliminary analysis suggests that alternate formulations could, however, be developed to estimate POM deposition using overlying water concentrations of POC or Chl-a and accounting for seasonal changes in C:CHL, sinking velocity, and turbulence. Secondly, the use of fitting POM deposition to observed NH_4^+ fluxes assumes a constant C:N ratio. Because C:N ratios can vary spatially and seasonally (e.g., Burdige and Zheng, 1998), this could limit the ability of SFM to simulate diagenesis and solute fluxes across time and space. In addition, SFM does not include benthic algae and the associated photosynthetic and respiratory processes, which seriously limits its use for shallow clear-water systems. Previous studies have, however, demonstrated that these processes can be readily incorporated into SFM (Cerco and Seitzinger, 1997). Although temperature dependency functions in SFM are appropriate for many temperate coastal systems, they may need to be re-calibrated for tropical or cold-water environments. Lastly, SFM's two-layer vertical resolution limits its ability to simulate fine scale vertically separated processes; however, the elegant simplicity of this scheme (e.g., Billen et al., 1989) adds to the model's flexibility as a linked component in 3D biophysical models and as a tool in stand-alone applications.

4.6. Highlights

This paper illustrates the simulation skill and flexibility of application for the stand-alone version of SFM with a focus on analyzing sediment–water fluxes of NH_4^+, NO_3^-, N_2 and O_2. The model uses an efficient two-layer structure and a formal accounting of key biogeochemical processes to compute mixing and reaction rates within the sediment and solute fluxes across the sediment–water interface. Here we have demonstrated a range of ways that the model can complement field measurements to estimate unmeasured processes, missing data and boundary conditions, and it can be used to address research questions about sediment diagenesis through scenario simulations. A few specific examples are mentioned below to highlight the value of this model.

- Rates of POM deposition, which are difficult and expensive to measure in shallow coastal waters, can be estimated using SFM in conjunction with seasonal and regional measurements of sediment–water NH_4^+ fluxes. In this study we found that model-calculated rates of annual mean POM deposition closely matched estimates from field deployments of sediment traps, and interannual variations in modeled POM deposition agreed well with field rates derived from sediment chlorophyll-*a* distributions.
- Robust model validation has been demonstrated using multiple lines of evidence and types of field data including porewater NH_4^+ concentrations, sediment–water NH_4^+ fluxes, labile sediment carbon content, sediment oxygen demand, and sulfate reduction rates.
- With data on overlying water concentrations and sediment–water fluxes of NH_4^+, NO_3^-, and O_2, the model can be used to compute key unmeasured processes like denitrification and sulfate reduction.

Acknowledgments

We would like to thank William Ball, Jeffrey Cornwell, James Fitzpatrick, Ming Li, Yun Li, Eva Bailey and Rebecca Murphy for the many discussions we have had related to topics covered in this manuscript. Comments from two anonymous reviewers substantially improved the clarity and quality of this manuscript. We would also like to thank the United States Environmental Protection Agency Chesapeake Bay Program and the Maryland Department of Natural Resources for collecting many of the data presented in this work. Partial funding for our contribution to this work came from the United States National Oceanographic and Atmospheric Administration (NOAA) Coastal Hypoxia Research Program (CHRP-NAO7NOS4780191), the National Science Foundation-funded Chesapeake Bay Environmental Observatory (CBEO-3 BERS-0618986), and by the State of Maryland Department of Natural Resources (K00B920002). This work is NOAA Coastal Hypoxia Research Program (CHRP) Publication # 175 and the University of Maryland Center for Environmental Science Publication # 4705.

References

Balzer, W., 1996. Particle mixing processes of Chernobyl fallout in deep Norwegian Sea sediments: evidence for seasonal effects. Geochimica et Cosmochimica Acta 60, 3425–3433.

Berg, P., Risgaard-Petersen, N., Rysgaard, S., 1998. Interpretation of measured concentration profiles in sediment pore water. Limnology and Oceanography 43, 1500–1510.

Billen, G., Dessery, S., Lancelot, C., Meybeck, M., 1989. Seasonal and inter-annual variations of nitrogen diagenesis in the sediments of a recently impounded basin. Biogeochemistry 8, 73–100.

Blackburn, T.H., Blackburn, N.D., Jensen, K., Risgaardpetersen, N., 1994. Simulation model of the coupling between nitrification and denitrification in freshwater sediment. Applied and Environmental Microbiology 60, 3089–3095.

Boesch, D.F., Brinsfield, R.B., Magnien, R.E., 2001. Chesapeake Bay eutrophication: scientific understanding, ecosystem restoration, and challenges for agriculture. Journal of Environmental Quality 30, 303–320.

Boudreau, B.P., 1991a. Modeling the sulfide oxygen reaction and associated pH gradients in porewaters. Geochimica et Cosmochimica Acta 55, 145–159.

Boudreau, B.P., 1991b. Modelling the sulfide-oxygen reaction and associated pH gradients in porewaters. Geochimica et Cosmochimica Acta 55, 145–159.

Boynton, W.R., Bailey, E.M., 2008. Sediment Oxygen and Nutrient Exchange Measurements from Chesapeake Bay, Tributary Rivers and Maryland Coastal Bays: Development of a Comprehensive Database & Analysis of Factors Controlling Patterns and Magnitude of Sediment-Water Exchanges. University of Maryland Center for Environmental Science Technical Report Series No. TS-542-08, Solomons, MD.

Bricker, O.P., Matisoff, G., Holden, G.R., 1977. Interstitial water chemistry of Chesapeake Bay sediments. Basic Data Report No. 9, Maryland Geological Survey, Annapolis, MD.

Buesseler, K.O., Antia, A.N., Chen, M., Fowler, S.W., Gardner, W.D., Gustafsson, O., Harada, K., Michaels, A.F., Rutgers van der Loeff, M., Sarin, M., 2007. An assessment of the use of sediment traps for estimating upper ocean particle fluxes. Journal of Marine Research 65, 345–416.

Burdige, D.J., 1991. The kinetics of organic matter mineralization in anoxic marine sediments. Journal of Marine Research 49, 727–761.

Burdige, D.J., Zheng, S.L., 1998. The biogeochemical cycling of dissolved organic nitrogen in estuarine sediments. Limnology and Oceanography 43, 1796–1813.

Buring, A.J., Hamilton, S.K., 2007. Have we overemphasized the role of denitrification in aquatic ecosystems? A review of nitrate removal pathways. Frontiers in Ecology and the Environment 5, 89–96.

Cai, W.-J., Sayles, F.L., 1996. Oxygen penetration depths and fluxes in marine sediments. Marine Chemistry 52, 123–131.

Cai, W.J., Luther, G.W., Cornwell, J.C., Giblin, A.E., 2010. Carbon cycling and the coupling between proton and electron transfer reactions in aquatic sediments in Lake Champlain. Aquatic Geochemistry 16, 421–446.

Cerco, C.F., 1995. Simulation of long-term trends in Chesapeake Bay eutrophication. Journal of Environmental Engineering 121, 298–310.

Cerco, C.F., Cole, T., 1993. Three-dimensional eutrophication model of Chesapeake Bay. Journal of Environmental Engineering ASCE 119, 1006–1025.

Cerco, C.F., Noel, M.R., 2005. Incremental improvements in Chesapeake Bay Environmental Model Package. Journal of Environmental Engineering 131, 745–754.

Cerco, C.F., Seitzinger, S.P., 1997. Measured and modeled effects of benthic algae on eutrophication in Indian River Rehoboth Bay, Delaware. Estuaries 20, 231–248.

Cloern, J.E., 2001. Our evolving conceptual model of the coastal eutrophication problem. Marine Ecology Progress Series 210, 223–253.

Conley, D.J., Carstensen, J., Vaquer, R., Duarte, C.M., 2009. Ecosystem thresholds with hypoxia. Hydrobiologia 629, 21–29.

Conley, D.J., Markager, S., Andersen, J., Ellermann, T., Svendsen, L.M., 2002. Coastal eutrophication and the Danish National Aquatic Monitoring and Assessment Program. Estuaries 25, 848–861.

Cowan, J.L., Pennock, J.R., Boynton, W.R., 1996. Seasonal and interannual patterns of sediment-water nutrient and oxygen fluxes in Mobile Bay, Alabama (USA): regulating factors and ecological significance. Marine Ecology Progress Series 141, 229–245.

Cowan, J.L.W., Boynton, W.R., 1996. Sediment-water oxygen and nutrient exchanges along the longitudinal axis of Chesapeake Bay: seasonal patterns, controlling factors and ecological significance. Estuaries 19, 562–580.

Dhakar, S.P., Burdige, D.J., 1996. Coupled, non-linear, steady state model for early diagenetic processes in pelagic sediments. American Journal of Science 296, 296–330.

Di Toro, D.M., 2001. Sediment Flux Modeling. Wiley-Interscience, New York.

Di Toro, D.M., Fitzpatrick, J.J., 1993. Chesapeake Bay Sediment Flux Model. Chesapeake Bay Program Office, U.S. Environmental Protection Agency and U.S. Army Engineer District, Baltimore, Annapolis, Maryland and Baltimore, Maryland, p. 316.

Diaz, R.J., Rosenberg, R., 1995. Marine benthic hypoxia: a review of its ecological effects and the behavioural responses of benthic macrofauna. Oceanography and Marine Biology: An Annual Review 33, 245–303.

Diaz, R.J., Rosenberg, R., 2008. Spreading dead zones and consequences for marine ecosystems. Science 321, 926–929.

Emerson, S., Jahnke, R., Heggie, D., 1984. Sediment water exchange in shallow water estuarine sediments. Journal of Marine Research 42, 709–730.

Fennel, K., Brady, D., DiToro, D., Fulweiler, R.W., Gardner, W.S., Giblin, A., McCarthy, M.J., Rao, A., Seitzinger, S., Thouvenot-Korppoo, M., Tobias, C., 2009. Modeling denitrification in aquatic sediments. Biogeochemistry 93, 159–178.

Fennel, K., Wilkin, J., Levin, J., Moisan, J., O'Reilly, J., Haidvogel, D., 2006. Nitrogen cycling in the Middle Atlantic Bight: results from a three-dimensional model and implications for the North Atlantic nitrogen budget. Global Biogeochemical Cycles 20.

Fitzpatrick, J.J., 2009. Assessing skill of estuarine and coastal eutrophication models for water quality managers. Journal of Marine Systems 76, 195–211.

Fulweiler, R.W., Nixon, S.W., Buckley, B.A., Granger, S.L., 2007. Reversal of the net dinitrogen gas flux in coastal marine sediments. Nature 448, 180–182.

Gardner, W.S., McCarthy, M.J., An, S.M., Sobolev, D., Sell, K.S., Brock, D., 2006. Nitrogen fixation and dissimilatory nitrate reduction to ammonium (DNRA) support nitrogen dynamics in Texas estuaries. Limnology and Oceanography 51, 558–568.

Grote, A., 1934. Der Sauerstoffhaushalt der Seen. Die Binnengewasser 14, 217.

Gust, G., Kozerski, H.P., 2000. *In situ* sinking-particle flux from collection rates of cylindrical traps. Marine Ecology Progress Series 208, 93–106.

Gypens, N., Lancelot, C., Soetaert, K., 2008. Simple parameterisations for describing N and P diagenetic processes: application in the North Sea. Progress In Oceanography 76, 89–110.

Hagy, J.D., Boynton, W.R., Jasinski, D.A., 2005. Modelling phytoplankton deposition to Chesapeake Bay sediments during winter-spring: interannual variability in relation to river flow. Estuarine, Coastal and Shelf Science 62, 25–40.

Hakanson, L., Floderus, S., Wallin, M., 1989. Sediment trap assemblages – a methodological description. Hydrobiologia 176, 481–490.

Heip, C.H.R., Goosen, N.K., Herman, P.M.J., Kromkamp, J., Middelburg, J.J., Soetaert, K., 1995. Production and consumption of biological particles in temperate tidal estuaries. In: Ansell, A.D., Gibson, R.N., Barnes, M. (Eds.), Oceanogr. Mar. Biol. Annu. Rev. University College London Press, London, pp. 1–149.

Hetland, R.D., DiMarco, S.F., 2008. How does the character of oxygen demand control the structure of hypoxia on the Texas-Louisiana continental shelf? Journal of Marine Systems 70, 49–62.

Hooke, R., Jeeves, T.A., 1961. 'Direct search' solution of numerical and statistical problems. Journal of the Association for Computing Machinery (ACM) 8, 212–229.

Howarth, R.W., Jorgensen, B.B., 1984. Formation of ^{35}S-labelled elemental sulfur and pyrite in coastal marine sediments (Limfjorden and Kysing Fjord, Denmark) $^{35}SO_4^{2-}$ during short-term reduction measurements. Geochimica et Cosmochimica Acta 48, 1807–1818.

Hutchinson, G., 1957. A treatise on limnology. In: Part 2-Chemistry in Lakes, vol. 1. John Wiley & Sons, New York.

Jenkins, M.C., Kemp, W.M., 1984. The coupling of nitrification and denitrification in two estuarine sediments. Limnology and Oceanography 29, 609–619.

Jensen, M.H., Lomstein, E., Sorensen, J., 1990. Benthic NH_4^+ and NH_3^- flux following sedimentation of a spring phytoplankton bloom in Aarhus Bight, Denmark. Marine Ecology Progress Series 61, 87–96.

Jiang, M.S., Zhou, M., 2008. Massachusetts Bay Eutrophication Model: 2005 Simulation. Massachusetts Water Resources Authority, p. 82.

Jorgensen, B.B., Revsbech, N.P., 1985. Diffusive boundary layers and the oxygen uptake of sediments and detritus. Limnology and Oceanography 30, 111–122.

Kemp, W.M., Sampou, P.A., Caffrey, J.M., Mayer, M., Henriksen, K., Boynton, W.R., 1990. Ammonium recycling versus denitrification in Chesapeake Bay sediments. Limnology and Oceanography 35, 1535–1563.

Kamp-Nielsen, L., 1992. Benthic-pelagic coupling of nutrient metabolism along an estuarine eutrophication gradient. Hydrobiologia 235/236, 457–470.

Kelly, J.R., Berounsky, V.M., Nixon, S.W., Oviatt, C.A., 1985. Benthic-pelagic coupling and nutrient cycling across an experimental eutrophication gradient. Marine Ecology Progress Series 26, 207–219.

Kelly, J.R., Nixon, S.W., 1984. Experimental studies of the effect of organic deposition on the metabolism of a coastal marine bottom community. Marine Ecology Progress Series 17, 157–169.

Kemp, W.M., Boynton, W.R., 1984. Spatial and temporal coupling of nutrient inputs to estuarine primary production: the role of particulate transport and decomposition. Bulletin of Marine Science 35, 522–535.

Kemp, W.M., Boynton, W.R., 1992. Benthic-pelagic interactions: nutrient and oxygen dynamics. In: Smith, D.E., Leffler, M., Mackiernan, M. (Eds.), Dissolved Oxygen in Chesapeake Bay: A Synthesis of Recent Research. Maryland Sea Grant College Park, Maryland, pp. 149–221.

Kemp, W.M., Brooks, M., Hinkle, D., 2007. Plankton Controls on Suspended Sediments and Water Clarity: Empirical Models Describing Interactions in Chesapeake Bay. Maryland Department of the Environment, Baltimore, MD, p. 60.

Kemp, W.M., Faganeli, J., Puskaric, S., Smith, E.M., Boynton, W.R., 1999. Pelagic-benthic coupling and nutrient cycling. In: Malone, T.C., Malej, A., Harding, L.W., Smodlaka, N., Turner, R.E. (Eds.), Ecosystems at the Land-Sea Margin: Drainage Basin to Coastal Sea. American Geophysical Union, Washington, DC, pp. 295–339.

Kemp, W.M., Sampou, P.A., Garber, J., Tuttle, J., Boynton, W.R., 1992. Seasonal depletion of oxygen from bottom waters of Chesapeake Bay: roles of benthic and planktonic respiration and physical exchange processes. Marine Ecology Progress Series 85, 137–152.

Koop-Jakobsen, K., Giblin, A.E., 2010. The effect of increased nitrate loading on nitrate reduction via denitrification and DNRA in salt marsh sediments. Limnology and Oceanography 55, 789–802.

Kozerski, H.P., 1994. Possibilities and limitations of sediment traps to measure sedimentation and resuspension. Hydrobiologia 284, 93–100.

Lin, J., Xie, L., Pietrafesa, L.J., Ramus, J.S., Paerl, H.W., 2007. Water quality gradients across Albemarle-Pamlico Estuarine System: seasonal variations and model applications. Journal of Coastal Research 23, 213–229.

Malone, T.C., Crocker, L.H., Pike, S.E., Wendler, B.W., 1988. Influence of river flow on the dynamics of phytoplankton production in a partially stratified estuary. Marine Ecology Progress Series 48, 235–249.

Marsho, T.V., Burchard, R.P., Fleming, R., 1975. Nitrogen fixation in Rhode River estuary of Chesapeake Bay. Canadian Journal of Microbiology 21, 1348–1356.

Marvin-DiPasquale, M.C., Boynton, W.R., Capone, D.G., 2003. Benthic sulfate reduction along the Chesapeake Bay central channel. II. Temporal controls. Marine Ecology Progress Series 260, 55–70.

Marvin-DiPasquale, M.C., Capone, D.G., 1998. Benthic sulfate reduction along the Chesapeake Bay central channel. I. Spatial trends and controls. Marine Ecology Progress Series 168, 213–228.

Matisoff, G., Wang, X.S., 1998. Solute transport in sediments by freshwater infaunal bioirrigators. Limnology and Oceanography 43, 1487–1499.

McGlathery, K.J., Sundbäck, K., Anderson, I.C., 2007. Eutrophication in shallow coastal bays and lagoons: the role of plants in the coastal filter. Marine Ecology Progress Series 348, 1–18.

Middelburg, J.J., Levin, L.A., 2009. Coastal hypoxia and sediment biogeochemistry. Biogeosciences 6, 1273–1293.

Miller, D.C., Geider, R.J., MacIntyre, H.L., 1996. Microphytobenthos: the ecological role of the "secret garden" of unvegetated, shallow-water marine habitats. II. Role in sediment stability and shallow-water food webs. Estuaries 19, 202–212.

Morse, J.W., Millero, F.J., Cornwell, J.C., Rickard, D., 1987. The chemistry of the hydrogen-sulfide and iron sulfide systems in natural waters. Earth-Science Reviews 24, 1–42.

Mulder, A., Vandegraaf, A.A., Robertson, L.A., Kuenen, J.G., 1995. Anaerobic ammonium oxidation discovered in a denitrifying fluidized-bed reactor. FEMS Microbiology Ecology 16, 177–183.

Nixon, S.W., 1981. Remineralization and nutrient cycling in coastal marine ecosystems. In: Neilson, B.J., Cronin, L.E. (Eds.), Estuaries and Nutrients. Humana Press, Clifton, NJ, pp. 111–138.

Nixon, S.W., 1995. Coastal marine eutrophication: a definition, social causes, and future concerns. Ophelia 41, 199–219.

Rich, J.J., Dale, O.R., Song, B., Ward, B.B., 2008. Anaerobic ammonium oxidation (Anammox) in Chesapeake Bay sediments. Microbial Ecology 55, 311–320.

Robbins, J.A., Keilty, T., White, D.S., Edgington, D.N., 1989. Relationships among tubificid abundances, sediment composition, and accumulation rates in Lake Erie. Canadian Journal of Fisheries and Aquatic Sciences 46, 223–231.

Roden, E.E., Tuttle, J.H., 1996. Carbon cycling in mesohaline Chesapeake Bay sediments 2: kinetics of particulate and dissolved organic carbon turnover. Journal of Marine Research 54, 343–383.

Roden, E.E., Tuttle, J.H., Boynton, W.R., Kemp, W.M., 1995. Carbon cycling in mesohaline Chesapeake Bay sediments 1: POC deposition rates and mineralization pathways. Journal of Marine Research 53, 799–819.

Scully, M.E., 2010. Wind modulation of dissolved oxygen in Chesapeake Bay. Estuaries and Coasts 33, 1164–1175.

Soetaert, K., Herman, P.M.J., Middelburg, J.J., 1996. Dynamic response of deep-sea sediments to seasonal variations: a model. Limnology and Oceanography 41, 1651–1668.

Soetaert, K., Middelburg, J.J., 2009. Modeling eutrophication and oligotrophication of shallow-water marine systems: the importance of sediments under stratified and well-mixed conditions. Eutrophication in Coastal Ecosystems, 239–254.

Sohma, A., Sekiguchi, Y., Kuwae, T., Nakamura, Y., 2008. A benthic-pelagic coupled ecosystem model to estimate the hypoxic estuary including tidal flat–Model description and validation of seasonal/daily dynamics. Ecological Modelling 215, 10–39.

Stow, C.A., Jolliff, J., McGillicuddy, D.J., Doney, S.C., Allen, J.I., Friedrichs, M.A.M., Rose, K.A., Wallheadg, P., 2009. Skill assessment for coupled biological/physical models of marine systems. Journal of Marine Systems 76, 4–15.

Tal, Y., Watts, J.E.M., Schreier, H.J., 2005. Anaerobic ammonia-oxidizing bacteria and related activity in Baltimore inner Harbor sediment. Applied and Environmental Microbiology 71, 1816–1821.

Testa, J.M., Kemp, W.M., 2012. Hypoxia-induced shifts in nitrogen and phosphorus cycling in Chesapeake Bay. Limnology and Oceanography 57, 835–850.

Testa, J.M., Brady, D.C., Di Toro, D.M. Boynton, W.R., Kemp, W.M., Sediment flux modeling: simulating nitrogen, phosphorus, and silica cycles, in press.

Westrich, J.T., Berner, R.A., 1984. The role of sedimentary organic matter in bacterial sulfate reduction: the G model tested. Limnology and Oceanography 29, 236–249.